Epidermal Electronics

Dae-Hyeong Kim[1⊥], Nanshu Lu[1⊥], Rui Ma[2⊥], Yun-Soung Kim[1], Rak-Hwan Kim[1], Shuodao Wang[3], Jian Wu[3], Sang Min Won[1], Hu Tao[4], Ahmad Islam[1], Ki Jun Yu[1], Tae-il Kim[1], Raeed Chowdhury[2], Ming Ying[1], Lizhi Xu[1], Ming Li[3,6], Hyun-Joong Chung[1], Hohyun Keum[1], Martin McCormick[2], Ping Liu[5], Yong-Wei Zhang[5], Fiorenzo G. Omenetto[4], Yonggang Huang[3], Todd Coleman[2], John A. Rogers[1*]

[1]*Department of Materials Science and Engineering, Beckman Institute for Advanced Science and Technology, and Frederick Seitz Materials Research Laboratory, University of Illinois at Urbana-Champaign, Urbana, IL 61801 USA*
[2]*Department of Electrical and Computer Engineering, Coordinated Science Laboratory, University of Illinois at Urbana-Champaign, Urbana, IL 61801, USA*
[3]*Department of Mechanical Engineering and Department of Civil and Environmental Engineering, Northwestern University, Evanston, IL 60208, USA*
[4]*Department of Biomedical Engineering, Tufts University, Medford, MA 02155, USA*
[5]*Institute of High Performance Computing, 1 Fusionopolis Way, #16-16 Connexis, 138632, Singapore.*
[6]*State Key Laboratory of Structural Analysis for Industrial Equipment, Dalian University of Technology, Dalian 116024, China.*

[⊥] *D.-H. Kim, N. Lu and R. Ma contributed equally.*

*To whom correspondence should be addressed. *E-mail:* jrogers@uiuc.edu

One sentence summary: Advanced materials and device designs enable electronic systems with physical properties matched to the epidermis, suitable as a versatile class of skin-integrated technology for applications in physiological status monitoring, wound measurement/treatment, human/machine interfaces, covert communications and others.

Abstract

We report materials, mechanics principles and designs layouts for electronic systems that achieve thicknesses (~30 μm), effective elastic moduli (<150 kPa), bending stiffnesses (<1 nN·m) and areal mass densities (< 3.8 mg/cm^2) matched to the epidermis. Laminating such devices onto the skin leads to conformal contact, intimate integration and adequate adhesion based on van der Waals interactions alone, in a manner that is mechanically invisible to the user. We describe a diverse collection of devices in this format, ranging from elecrophysiological (EP), temperature and strain sensors, to transistors, light emitting diodes, photodetectors and a variety of components capable of radio frequency operation, including inductors, capacitors, oscillators and rectifying diodes. Silicon solar cells and wireless inductive coils provide options for power supply. As systems-level demonstrators of this technology, we report skin-mounted, amplified monitors of EP activity produced by the heart, brain and skeletal muscles. Data collected with such devices contain sufficient information for meaningful human/machine interfaces, as we illustrate with an unusual type of computer game controller.

Physiological measurement and stimulation techniques that exploit interfaces to the skin have been of interest for more than 40 years, the former beginning in 1966 with electromyography of laryngeal muscles *(1-3)*. Despite much progress over this time, nearly all associated device technologies continue to rely on conceptually old designs. Typically, small numbers of bulk electrodes mount on the skin via adhesive tapes, mechanical clamps/straps and/or penetrating needles, often mediated by conductive gels, with terminal connections to separate boxes that house collections of rigid circuit boards, power supplies and communication components *(4-9)*. These systems have many important capabilities, but they are poorly suited for practical application outside of research labs or clinical settings, due to difficulties in establishing long-lived, robust electrical contacts that do not irritate the skin, and in achieving integrated systems with overall sizes, weights and shapes that do not cause discomfort during prolonged use *(8,9)*. Here we introduce a different approach, in which the electrodes, electronics, sensors, power supply and communication components are configured together into ultrathin, low modulus, lightweight, stretchable 'skin-like' membranes that conformally laminate onto the surface of the skin by soft contact, in a manner that is mechanically invisible to the user, much like a temporary transfer tattoo.

Figure 1 shows a demonstration platform for the individual components of such a technology, including a collection of multifunctional sensors (e.g. temperature, strain, electrophysiological), microscale light emitting diodes (LEDs), active/passive circuit elements (e.g. transistors, diodes, resistors), wireless power coils and devices for radio frequency (RF) communications (e.g. high frequency inductors, capacitors, oscillators and antennae), all integrated on the surface of a thin (~30 μm), gas-permeable elastomeric sheet based on a modified polyester (PE; BASF, Germany) with low Young's modulus (~60 kPa, Fig. S1A). The devices and interconnects exploit ultrathin layouts (<7 μm), neutral mechanical plane (NMP) configurations and optimized geometrical designs. The active elements use established electronic materials such as silicon and gallium arsenide, in the form of filamentary serpentine nanoribbons and micro/nanomembranes. The result is a high performance system that offers reversible, elastic responses to large strain deformations with effective moduli, bending stiffnesses and areal mass densities that are orders of magnitude smaller than those possible with conventional electronics, or even with recently explored flexible/stretchable device technologies *(10-19)*. These and other key physical properties are, in fact, comparable to those of the skin itself. Water-soluble polymer sheets (polyvinyl alcohol; PVA, Aicello, Japan; Young's modulus ~1.9 GPa, thickness ~ 50 μm (Fig. S1B)), serve as temporary supports for manual mounting of these systems on the skin, in an overall construct that is directly analogous to that of a temporary transfer tattoo. The top frame of Fig. 1B provides an image of a device like the one in Fig. 1A, after integrating it onto the skin by washing away the PVA and then partially peeling it back using a pair of tweezers. When completely removed, the system collapses on itself due to its extreme deformability and 'skin-like' physical properties, as shown in the bottom frame of Fig. 1B. (See SOM Movie S1.) The schematic illustration in the inset shows an approximate cross sectional layout.

These mechanical characteristics lead to robust adhesion to the skin via van der Waals forces alone, without any mechanical fixturing hardware or adhesive tapes. The devices impose negligible mechanical or mass loading, as is evident from the images of Fig. 1C, which show the skin deforming freely and reversibly, without any apparent constraints in motion due to the devices. Electronics in this form can even be integrated directly with commercial temporary transfer tattoos, as a substrate alternative to PE/PVA. The result, shown in Fig. 1D, is of possible interest as a way to conceal the active components and/or to exploit low cost materials (i.e. substrate, adhesives, backing layers) already developed for temporary transfer tattoos. (See SOM Movie S2 for details.) Potential uses include physiological status monitoring, wound measurement/treatment, biological/chemical sensing, human-machine interfaces, covert communications and others.

Understanding the mechanics of this kind of device, the mechanophysiology of the skin, and the behavior of the coupled abiotic-biotic system, are all critically important. For present purposes, the skin can be approximated as a bilayer, consisting of the epidermis (modulus: 140-600 kPa; thickness 0.05-1.5 mm) and the dermis (modulus: 2-80 kPa; thickness 0.3-3 mm) *(20-23)*. This bilayer exhibits linear elastic response to tensile strains <~15%, which transitions to non-linear behavior at higher strains, with adverse, irreversible effects beyond 30% *(24)*. The surface of the skin typically has natural wrinkles, creases and pits with amplitudes and feature sizes of 15-100 μm *(25)* and 40-1000 μm *(26)*, respectively. The devices described here (i.e. Fig. 1) have moduli, thicknesses and other physical properties that are well matched to the epidermis itself, with the ability to conform to the relief on its surface. We therefore refer to this class of technology as an ‘epidermal electronic system’ (EES).

Macroscopically, EES on skin can be treated as a thin film on an epidermis/dermis bilayer substrate. Microscopically, the sizes of the individual electronic components and interconnects are comparable to those of relief features on the skin, and therefore must be considered explicitly. Multi-scale analysis and experimental measurements can capture the detailed behaviors. We begin by considering aspects of adhesion, in the macroscopic limit. Globally, detachment can occur in either tension or compression, due to interfacial cracks that initiate at the edges or the central regions of the EES, respectively. Low effective moduli and small thicknesses minimize the deformation-induced stored elastic energy that drives both of these failure modes. Analytical calculation (SOM) shows that compared to silicon chips (thickness ~1 mm) and sheets of polyimide (thickness ~75 μm), the driving forces for delamination of the EES/skin interface are reduced by more than five orders of magnitude. The values are so small, in fact, that adequate adhesion is possible, immediately upon lamination, due simply to van der Waals interactions. Figure 2A shows measurements and theoretical calculations (SOM) that explore the relevant scaling behaviors, in structures that provide simplified, macroscopic models of EES/skin. The experiments use sheets of PE (~2 mm thick) for the skin and films of poly(dimethylsiloxane) (PDMS, Dow Corning, USA) for the EES. Figure 2A plots the critical delamination strain as a function of PDMS thickness, for two different formulations: one with a modulus of 19 kPa (50:1) and the other 145 kPa (30:1, Fig. S1C). The results confirm that reducing the modulus and thickness lowers the forces that drive interface delamination, for a given applied strain (bending or stretching), without lower bound.

To explore the limits, consider that the mechanical properties of the EES depend on the effective modulus and thickness of both the circuits/sensors and the substrate. In samples like those in Fig. 1, the properties of the active components and interconnects can dominate the mechanics of the overall system. The in-plane layouts and materials of this layer are, therefore, key design parameters. Recent work in stretchable electronics establishes that the overall range of deformability can be optimized in systems composed of active devices joined together in open mesh structures by non-coplanar interconnects in NMP configurations, where elastomers with relatively large modulus (2-10 MPa) and thickness (mm's to cm's) serve as substrates *(13, 14)*. For EES, the effective modulus (E_{EES}) and bending stiffness ($\overline{EI}_{\mathrm{EES}}$), rather than the range of stretchability, are paramount. These requirements demand alternative designs and choices of materials. If we assume that the moduli of the individual devices (e.g. ~160 GPa for Si and ~90 GPa for GaAs) are much higher than the compliance of the interconnects, then we can write the approximate expression $E_{\mathrm{EES}} = E_{\mathrm{int}}\,(1 + L_{\mathrm{d}} / L_{\mathrm{s}})$, which has been verified by the finite element method (FEM), where E_{int} is the effective modulus of the interconnects, L_{d} is the characteristic device size, and L_{s} is the distance between devices, as illustrated in Fig. S1D. The value of E_{EES} can be minimized by reducing E_{int} and $L_{\mathrm{d}} / L_{\mathrm{s}}$. For the former, thin, narrow interconnect lines, formed into large-amplitude, 'filamentary serpentine' (FS) shapes represent effective designs. For the latter, ultrathin active devices that adopt similar FS layouts and continuously integrate with FS interconnects reduce the effective value of L_{d} to zero. The value of $\overline{EI}_{\mathrm{EES}}$ decreases rapidly with the thicknesses of the devices, interconnects and substrate. Figure 2B (left frame) shows an ultrathin FS construct, with a cross sectional schematic illustration as an inset. Results of tensile testing (right frame of Fig. 2B) indicate that such FS-EES samples (left frame of Fig. 2B) achieve E_{EES} (~140 kPa) and $\overline{EI}_{\mathrm{EES}}$ (~0.3 nN·m, calculation shown in SOM) that are comparable to the epidermis, and more than one and five orders of magnitude smaller than previously reported stretchable electronic devices, respectively *(27)*. Furthermore, highly repeatable loading and unloading stress-strain curves up to strains of 30% demonstrate the pure elastic response of the FS-EES, with a range of stretchability that is much larger than that of the epidermis. Such highly elastic FS layouts can maintain nearly 20% areal contact of active elements with the skin, for effective electrical interfaces. FEM captures quantitatively the strains and stresses in FS-EES, as a function of induced deformation, as shown in Fig. 2C for stretching to ~30% strain along the x (left) and y (right) directions. In both cases, the maximum principal strains in the metal are less than ~0.2%. The same calculations yield effective tensile moduli (Fig. 2B, right frame), with excellent correspondence to experiment. In certain applications, layouts that involve some combination of FS geometries and device islands (i.e. L_d not equal to zero) connected by FS interconnects (e.g. Fig. 1 and Fig. S1E) can be used, with expected consequences on the local mechanics (Fig. S1F). In both options, suitable designs lead to mechanical and adhesive properties that allow conformal adhesion to the skin and minimal loading effects (Fig. 2D). Without optimized layouts, we observe delamination under similar conditions of deformation (See SOM Movie S3), consistent with the fracture modes illustrated in Fig. 2A.

For many uses of EES, physical coupling of electrodes to the surface of the skin is important. Microscopic characterization and modeling of the skin-EES interface provides some insights. Confocal micrographs of EES mounted on pig skin appear in Fig. 2E, F as well as Fig. S2C. With FS structures, the results show remarkably conformal contact, not only at the PE regions of the EES, but also at the FS elements (Fig. 2E, F). Similar behavior obtains, but in a less ideal fashion (Fig. S2C), with layouts that incorporate large device islands. These observations are consistent with analytical mechanics treatments that use macroscopic models of the EES and account for microscopic structures on the skin. Here, it can be shown (SOM) that contact will occur spontaneously, without an applied pressure, when

$$\frac{\pi \overline{E}_{\text{skin}} h_{\text{rough}}^{2}}{\gamma \lambda_{\text{rough}}} < 16 + \frac{\overline{E}_{\text{skin}} \lambda_{\text{rough}}^{3}}{\pi^{3} \overline{EI}_{\text{EES}}}, \tag{1}$$

where γ, $\overline{E}_{\text{skin}}$, h_{rough} and λ_{rough} are the effective work of adhesion, and the plane-strain modulus, roughness amplitude and wavelength of the skin, respectively. The scaling law in Eq. (1), which involves two dimensionless combinations of EES and skin properties, shows that EES with low bending stiffness, on smooth and soft skin with strong adhesion all promote conformal contact. Using experimental data and a measured value of $\gamma \sim 0.16$ N/m (SOM), this criterion implies that the FS-EES can conform to the skin, without applied pressure, when h_{rough} is <~50 μm (Fig. 2G) for $\lambda_{\text{rough}} = 140$ μm, consistent with observation in Fig. 2F where the roughness amplitude is 5~20 μm. Related calculations indicate that the contact pressure created by surface interactions is ~10 kPa (Fig. S10B), which is below the sensitivity of human skin (~20 kPa, *(28)*) but still sufficient to offer reasonable adhesion. (Improved bonding can be achieved by using adhesives that are built into platforms for temporary transfer tattoos, as in Fig. 1D). From a microscopic point of view, the soft, conformal nature of the EES helps to drive adhesion to the skin, with strongest effects in regions away from the devices and interconnects, where the local effective modulus is lowest. These interfacial forces assist in bringing neighboring FS structures into contact with the skin as well. Narrow, thin FS geometries facilitate this process. For materials and layouts explored here, the result is a total compressive force (per unit length) of ~-0.1 N/m for each FS strip. Calculations show that these interactions reduce the widths of the gaps between the PE and skin that exist proximal to the edges of the FS elements to < 0.2 μm, even for the thickest device structure (~3 μm) in experiments (Fig. S1E).

A key capability of EES is in monitoring electrophysiological (EP) processes related to activity of the brain (electroencephalograms; EEG), the heart (electrocardiograms; ECG) and muscle tissue (electromyograms; EMG). Amplified sensor electrodes that incorporate silicon metal oxide semiconductor field effect transistors (MOSFETs) in circuits where all components adopt FS designs provide devices for this purpose. Here, the gate of a FS-MOSFET connects to an extended FS electrode for efficient coupling to the body potential (Fig. 3A; the inset shows an analogous design based on a rectangular device island and FS interconnects), via contact with the skin, in a common-source amplifier configuration (Fig. 3B, left frame). Figure 3B (right frame) indicates the measured frequency response at different input capacitances (C_{IN}), in quantitative agreement with circuit simulations (Fig. S3A and B). The value of C_{IN} is determined by the sum of capacitances of gate electrode, the encapsulating PI and junction between the gate electrode and the body surface. The bandwidth matches requirements for high performance EP recording. A typical layout for this purpose includes four amplified channels, each comprised of a FS-MOSFET, a silicon-based FS resistor and an FS electrode. One channel provides a reference, while the others serve as sites for measurement. Results of demonstration experiments appear subsequently.

Many other classes of semiconductor devices and sensors are also possible in EES, including resistance-based temperature sensors built with meander electrodes of Pt (Fig. 3C left and Fig. S3C), in-plane strain gauges based on carbon-doped silicones (Fig. 3C right frame and Fig. S3D), LEDs and photodetectors based on AlInGaP (Fig. 3D left frame and Fig. S3E-G; for possible use in optical characterization of the skin/biofluids), and silicon FS photovoltaic cells (Fig. 3D right frame). Such cells can generate of a few tens of μW (Fig. S3H); increasing the areas or areal coverages can improve the output, but not without compromises in size and mechanics. Wireless powering via inductive effects represents an appealing alternative. Figure 3E shows an example of an FS inductive coil connected to a microscale InGaN LED, and electromagnetic modeling of its RF response. The resonance frequency (~35 MHz) matches that of a separately located transmission coil powered by an external supply. Voltage and current outputs in the receiver are sufficient to operate the microscale LEDs remotely, as shown in Fig. 3E. Such coils provide power directly in this example; they can also, conceivably, be configured to charge future classes of EES-integrated storage capacitors or batteries.

Figure 3F and G present examples of various RF components, of the type needed for wireless communications or for scavenging RF energy. Fig. 3F shows an optical image of silicon PIN diode (left frame) and its small-signal scattering parameters (right frame), indicating insertion loss (S21 in forward condition) of <6 dB and isolation (S21 in reverse condition) of >15 dB for frequencies up to 2 GHz. Examples of FS inductors and capacitors and their RF responses appear in Fig. 3F. Connecting pairs of such devices yields oscillators with expected resonant frequencies (Fig. 3F, lower right frame). A notable behavior is that the response varies with state of deformation, due the dependence of the RF inductance on geometry. For example, at tensile strains of ~12%, the resonance frequency shifts by ~30%. (Fig. S3I and J). Such effects, which also appear in the wireless power coils but not in the other devices of Fig. 3, will influence the behavior of antenna structures and certain related RF components. These issues must be considered explicitly in EES design and modes of operation.

EES configured for measuring ECG, EMG and EEG, in conformal, skin-mounted modes without conductive gels or penetrating needles provide important, system-level demonstrations of the ideas. ECG recordings from the chest reveal high quality signals with information on all phases of the heartbeat, including rapid depolarization of the cardiac wave, and the associated QRS complex (Fig. 4A, right frame) *(29)*. EMG measured on the leg, with muscle contractions to simulate walking and resting are presented in Fig. 4B, left frame. The measurements agree remarkably well with signals simultaneously collected using commercial, bulk tin electrodes that require conductive gels, mounted with tapes at the same location (Fig. 4B, right frame; Fig. S4). Figure 4C shows an alternative way to view the data (spectrogram), where the spectral content appears in a color contour plot with frequency and time along the y and x axes, respectively. Each muscle contraction corresponds to a red, vertical stripe that spans from 10 Hz to 300 Hz *(29)*.

To demonstrate EMG recording in a mode where conventional devices are particularly ill-suited, an EES mounted on the throat can monitor muscle activity, non-invasively, during speech (Fig. S5A). Here, recordings collected during vocalization of four words (“up”, “down”, “left” and “right”), repeated 10 times each (Fig. S6) exhibit distinctive patterns, as in Fig. 4D. Measurements from another set of words (“go”, “stop” and “great”; Fig. S5B and S7) suggest sufficient structure in the signals for recognizing a vocabulary of words. These capabilities create opportunities for EES-based human/machine interfaces. As an example, dynamic time warping pattern recognition algorithms applied to throat-based EMG data (Fig. 4D) enable control of a computer strategy game (Sokoban), as illustrated in Fig. 4E. The classifications occur in less than 3 s on a dual-core PC running codes in MATLAB, with an accuracy >90% (Fig. S8). Significant increases in speed are possible via optimized software and hardware implementations.

As a human/machine interface, EEG data offer additional promise, for use separately or together with EMG signals. EES mounted on a region of the forehead that is first prepared by exfoliating the stratum corneum using Scotch tape, yields reproducible, high quality results, as demonstrated in alpha rhythms recorded from awake subjects with their eyes closed (Fig. S9A). The expected feature at ~10 Hz appears clearly in the Fourier transformed data of Fig. 4F (left frame). The spectrogram of Fig. 4F (center) shows similar signatures during an experiment in which the subject's eyes are closed for first 10 seconds and then open for the next 10 seconds. The responses at ~10 and ~14 seconds correspond to eye opening and blinking, respectively. This activity disappears when the eyes are held open. The signal-to-noise ratios are comparable to those obtained in otherwise identical experiments using conventional, rigid bulk electrodes applied to the skin with conducting, coupling gels. In further demonstrations, EEG measured by EES reveal well-known cognitive phenomena such as the Stroop effect *(30, 31)*. In these experiments, subjects randomly presented with congruent or incongruent (Fig. S9B) colored words, whisper the color (not the word) as quickly as possible. The data show that the motor responses pertaining to the whispering are manifested by two peaks at ~650 ms (congruent case) and ~1000 ms (incongruent case) in the right frame of Fig. 4F. The time delay implies that the congruent stimuli require fewer cognitive resources and are quicker to process than the incongruent ones, consistent with the literature *(30, 31)*.

The materials and mechanics ideas presented in this report enable intimate, mechanically 'invisible', integration of high performance electronic functionality with the surface of the skin, in ways that bypass limitations of previous approaches. Further work to integrate the individual components reported here with one another and with additional ones such as power storage devices, could yield systems with expanded capabilities in sensing, computation, communication and others, for both healthcare and non-healthcare related applications. An important perspective is that many of the EES concepts are fully compatible with small-scale integrated circuits that can be released from ultrathin body silicon-on-wafer substrates. For long-term use, materials and device strategies to accommodate the continuous efflux of dead cells from the surface of the skin, and the processes of transpiration will also be needed. These and other challenges represent interesting opportunities for future research.

Figure Captions

Fig. 1 (**A**) Image of a multifunctional, 'skin-like' electronic system that serves as a demonstration platform for electrophysiological and temperature sensors, strain gauges, LEDs, wireless power coils, RF inductors, capacitors, diodes and oscillators, and a wireless transmit/receive antenna. Mounting this device on a sacrificial, water-soluble film of PVA, placing the entire structure against the skin, with electronics facing down, dissolving the PVA and then drying to remove the remaining water leaves the device conformally attached to the skin, in an overall procedure similar to that used for a temporary transfer tattoo. The elastic moduli, thickness and other physical properties of the device match the epidermis; we refer to the technology as an epidermal electronic system (EES). Adequate adhesion is possible through van der Waals forces alone, in a format that imposes negligible mass or mechanical loading effects on the skin. (**B**) EES partially (top frame) and fully (bottom frame) peeled away from the skin.

The inset shows a representative cross-sectional illustration of the structure, with the neutral mechanical plane (NMP) defined by a red dashed line. (**C**) Multifunctional EES on skin: undeformed (first frame), compressed (middle frame) and stretched (right frame). (**D**) A commercial temporary transfer tattoo provides an alternative to PE/PVA for the substrate; in this case, the system includes an adhesive to improve bonding to the skin. Images of the backside of a tattoo (first frame), electronics integrated onto this surface (second frame) and attached to skin with electronics facing down in undeformed (third frame) and compressed (fourth frame) states.

Fig. 2. (**A**) Plots of critical tensile (left frame) and compressive (right frame) strains for delamination of a test structure consisting of films of PDMS on substrates of PE, designed to model the EES/skin system. Data for formulations of PDMS with two different moduli are shown (red: 19 kPa; blue: 145 kPa). The results indicate that the critical strains increase as the PDMS thickness and modulus decrease, consistent with modeling results (lines). (**B**) Optical micrograph of an EES with filamentary serpentine (FS) design (left frame). The plot in the right frame shows the stress-strain data from uniaxial tensile measurements on an FS-EES, for two orthogonal directions. Data collected from a sample of pig skin are also presented. The FS-EES has modulus comparable to or less than the skin, over the range of strains shown here. The dashed lines correspond to calculations by finite element modeling. (**C**) Contour plots of strain distributions computed by FEM, for 30% tensile strains along x (left) and y (right). The results indicate maximum principle strains of less than 0.2% in the FS structures. (**D**) Skin of the forehead before (top left frame) and after integration of a representative FS-EES, at various magnifications and states of deformation. The dashed blue boxes in the right frames highlight

the outer boundary of the device. The red arrows indicate the direction of compressive strains, generated by contraction of facial muscles. The red dashed box in the upper right frame corresponds to the field of view of the image in the lower left. (**E**) Confocal microscope image (top view) of the contacting interface between an FS-EES and a sample of pig skin. The FS structure and the skin are dyed with red and blue fluorophores, respectively. (**F**) Cross-sectional confocal images, at locations corresponding to the numbered, white dashed lines shown in the top view frame above. The results indicate intimate, conformal contact, to within the resolution of the microscope. (**G**) Mechanics analysis of the condition for conformal contact as a function of FS-EES/skin adhesion and skin roughness.

Fig. 3. (**A**) Optical micrographs of an active electrophysiological (EP) sensor with local amplification, as part of an FS-EES. The left frame shows the source, drain and gate of a silicon MOSFET and a silicon feedback resistor before connection to sensor electrodes, all in FS layouts. The right image shows the final device, after metallization for the interconnects and sensor electrodes, with magnified view (inset). (**B**) Circuit diagram for the amplified EP sensor shown above (left frame). The right frame shows measured and simulated frequency response for different input capacitance ($C_{IN} = \infty$, 1μF, 220pF). (**C**) Optical micrograph of a temperature sensor that uses a platinum resistor with FS interconnects (left frame) and a strain guage that uses electrically conductive silicone (CPDMS; right frame). (**D**) Image of an array of microscale AlInGaP LEDs and photodetectors, in an interconnected array integrated on skin, under compressive deformation, (left frame) and of a FS silicon solar cell (right frame). (**E**) Image of a FS wireless coil, connected to a microscale AlGaN LED, powered by inductive coupling to a

separate transmission coil (not in the field of view). The right frame shows electromagnetic simulations of the behavior of the FS coil. (**F**) Optical micrograph of an interconnected pair of FS inductors and capacitors designed for RF operation (left top frame). The plot in the upper right shows the value of S21 measured on a set of FS capacitors as a function of frequency. The plot in the lower left frame shows the frequency dependence of S21 and S11 for an FS inductor. The graph on the bottom right shows resonant frequencies for LC oscillators built with different FS capacitors. (**G**) Image of a silicon RF diode (left frame) and the frequency dependence of S11 and S21 (right frame).

Fig. 4. (**A**) ECG signals measured with an EES integrated on the chest using an active EP sensor (left frame), and magnified view of data corresponding to a single heartbeat (right frame). (**B**) The left frame shows the results of EMG measurement using a similar device, mounted on the right leg during simulated walking (from 0 sec to 10 s) and standing (from 10 s to 20 s). The right frame shows similar data recorded using a conventional EMG sensor based on a tin electrode coupled to the skin with a conductive gel and affixed using adhesive tape. (**C**) Frequency spectral (i.e. spectrogram) representation of the data in (B), for each electrode type. (**D**) EMG spectrograms measured using an EES mounted on the neck during vocalization of four different words: "up", "down", "left" and "right". (**E**) Simulated video game control using pattern recognition algorithms applied to EMG data recorded with an EES on the neck. The yellow arrows indicate the direction of motion of the player icon from an initial position (red) to a final one (green). (**F**) The left frame shows discrete Fourier transform (DFT) coefficient associated with EES recordings of EEG from the forehead, showing expected alpha rhythms at

~10 Hz when the eyes are closed. (See SOM for DFT definition.) The center frame shows a spectrogram representation of the alpha rhythm measurement. The first and next 10 seconds correspond to periods when the eyes were closed and open, respectively. The right frame shows results that demonstrate expected Stroop effects in data measured with the same type of EES used for the alpha rhythms.

References and Notes

1. H. Berger, *Arch Psychiatr Nervenkr* **87**, 527 (1929).

2. C. Hardyck, L. Petrinovich, D. Elsworth, *Science* **154**, 1467 (1966).

3. E. J. Fox, R. Melzack, *Pain* **2**, 141 (1976).

4. J. G. Webster, in *Medical Instrumentation: Application and Design* (John Wiley & Sons, Inc., New York, 2009) p. 189-240.

5. A. Searle, L. Kirkup, *Physiol. Meas.* **21**, 271 (2001).

6. P. Griss, H. K. Tolvanen-Laakso, P. Meriläinen, G. Stemme, *IEEE Trans. Biomed. Eng.* **49**, 597 (2002).

7. L. M. Yu, F. E. H. Tay, D. G. Guo, L. Xu, K. L. Yap, *Sens. Actuators A* **151**, 17 (2009).

8. B. Gerdle, S. Karlsson, S. Day, M. Djupsjöbacka, in *Acquisition, Processing and Analysis of the Surface Electromyogram. Modern Techniques in Neuroscience*, U. Windhorst, H. Johansson Eds. (Springer Verlag, Berlin, 1999) p. 705-755.

9. J. R. Ives, S. M. Mirsattari, D. Jones, *Clinical Neurophysiol.* **118**, 1633 (2007).

10. T. Sekitani *et al.*, *Science* **321**, 1468 (2008).

11. S.C.B. Mannsfeld *et al.*, *Nat. Mater.* **9**, 859 (2010).

12. K. Takei *et al.*, *Nat. Mater.* **9**, 821 (2010).

13. D.-H. Kim *et al.*, *Science* **320**, 507 (2008).

14. R.-H. Kim *et al.*, *Nat. Mater.* **9**, 929 (2010).

15. M. Kubo *et al.*, *Adv. Mater.* **22**, 2749, (2010).

16. M. Gonzalez *et al.*, *Microelectronics Reliability* **48**, 825 (2008).

17. S. P. Lacour, J. Jones, S. Wagner, T. Li, Z. Suo, *Proc. IEEE.* **93,** 1459 (2005).

18. C. Keplinger, M. Kaltenbrunner, N. Arnold, S. Bauer, *Proc. Natl. Acad. Sci. USA.* **107**, 4505 (2010).

19. L. Hu *et al.*, *Nano Letters* **10**, 708 (2010).

20. Kuwazuru *et al.*, *Med. Eng. Physics* **30**, 516 (2008).

21. M. Geerligs, J. Biomech., *In press* (2011).

22. C. Pailler-Mattei *et al.*, *Med. Eng. Phy.* **30**, 599 (2008).

23. http://dermatology.about.com/cs/skinanatomy/a/anatomy.htm.

24. V. Arumugam, *J. Biosci.* **19**, 307 (1994).

25. L. Tchvialeva *et al.*, in *Skin Roughness Assessment. New Developments in Biomedical Engineering*, D. Campolo Eds. (InTech, http://www.intechopen.com/download/pdf/pdfs_id/9090, 2010) p. 346.

26. K.-P. Wilhelm, P. Elsner, E. Berardesca, in *Bioengineering of the Skin: Skin Surface Imaging and Analysis*, (CRC Press, Boca Raton, 1997) p. 154.

27. D.-H. Kim *et al.*, *Proc. Natl. Acad. Sci. USA.* **105**, 18675 (2008).

28. A. Kaneko, N. Asai, T. Kanda, *J. Hand Ther.* **18**, 421 (2005).

29. L. Sörnmo, P. Laguna, in *Bioelectrical Signal Processing in Cardiac and Neurological Applications*, (Elsevier, Amsterdam, 2005) p. 337-452.

30. J. R. Stroop, *J. Experimental Psychology* **18**, 643 (1935).

31. O. Spreen, E. A. Strauss, in *Compendium of Neuropsychological Tests: Administration, Norms and Commentary*, (Oxford University Press, New York, 2006) p. 477-499.

32. J. W. Hutchinson, Z. Suo, *Advances in Applied Mechanics* **29**, 63 (1992).

33. M. A. Biot., *Appl. Sci. Res. A* **12**, 168 (1963).

34. H. Jiang, Y. Sun, J. A. Rogers, Y. Huang, *Int. J. Solids Struct.* **45**, 2014 (2008).

35. Huang *et al.*, *Langmuir* **21**, 8058 (2005).

36. H. Tada, P. C. Paris, G. R. Irwin, in *The Stress Analysis of Cracks Handbook*, (ASME Press, New York, 2000) p. 161-162.

37. M. A. Meitl *et al.*, *Nat. Mater.* **5**, 33 (2006).

38. This material is based upon work supported by a National Security Science and Engineering Faculty Fellowship and a grant from the Air Force Research Laboratory, the National Science Foundation (NSF) under grant DMI-0328162 and it used facilities at the Materials Research Laboratory and Center for Microanalysis of Materials at the University of Illinois at Urbana-Champaign, suppored by the U.S. Department of Energy, Division of Materials Sciences under Award No. DE-FG02-07ER46471 and DE-FG02-07ER46453. N.L. acknowledges support from a Beckman Institute postdoctoral fellowship. Y.H. acknowledges NSF grants ECCS-0824129 and OISE-1043143.

Supporting Online Material

S1. Estimation of driving forces for interfacial delamination between devices and skin

Fracture mechanics of a linear elastic bilayer system *(32)* gives the steady-state driving force $G = \frac{1}{2} E h \varepsilon^2$ for interface delamination between a thin film of Young's modulus E and thickness h and a thick substrate under uniform tensile strain ε. For tensile/compressive strain of 1%, the driving forces for interface delamination of 1 mm-thick silicon (E = 180 GPa) and 75 μm-thick polyimide (E = 4 GPa) are 9×10^3 J/m^2 and 15 J/m^2, respectively. For EES (E = 150 kPa, h = 30 μm), the driving force is only 2.25×10^{-4} J/m^2 , which is more than five orders of magnitude lower than silicon or polyimide based devices.

S2. Sample preparation for confocal microscopy

To prepare samples for confocal microscopy, we stained the polymers and the pig skin with fluorescent dyes having distinct excitation and emission bands, as shown in Fig. S2A. Alexa 488 (Invitrogen) was used to stain the PE substrate. Ten grams of Alexa 488 powder was first dissolved in 300 μl DMSO (Dimethyl sulfoxide). Next, 1 μl of the 488-DMSO solution was diluted by 1 ml toluene and 100 μl of the resulting 488-DMSO-toluene solution was added to 2 ml Part A pre-polymer of 0030 Ecoflex. A magnetic stir bar was used to facilitate mixing, for 1 hour. We next added 2 ml Part B pre-polymer of Ecoflex and further mixed for 5 minutes. Spin coating this pre-polymer mixture at 3000 rpm onto a water-soluble PVA substrate and curing at room temperature for 4 hours and then at 70°C for 2 hours completed the preparation of PE. Alexa 647 was used to stain a film of polyimide, patterned into the shape of electronic circuitry. For the polyimide we dissolved ten grams of Alexa 647 powder into 300 μl DMSO. We then added 1 μl 647-DMSO to 1 ml NMP (N-Methylpyrrolidone) and mixed 10 μl of the resulting 647-DMSO-NMP solution into 1 ml of polyimide pre-polymer. As before, we used a magnetic stir bar to mix for 1 hour. Spin coating at 4000 rpm onto a PMMA coated Si wafer and bake at 250°C in glove box for 1 hour completed the preparation. Patterning the PI into desired structures of island-plus-serpentine and filamentary serpentine was accomplished by photolithography and dry etching. The final step involved transfer-printing the polyimide structure onto the PE(Ecoflex)-coated PVA substrate.

To stain the pig skin, we first mixed 10 gram FM 1-43FX into 300 μl DMSO. We then diluted 1μl FM-DMSO solution with 1 ml 1xPBS (Phosphate Buffered Saline). We rinsed a the pig skin in 1x PBS thoroughly. Applying a drop of the 1ml FM-DMSO-PBS solution onto the skin surface and waiting for 10 minutes produced the desired stain. Rinsing with 1x PBS removed excess dye. Fluorescent EES was then applied to stained pig skin sample by placing the device side against the surface of the skin and the gently spraying 1xPBS to dissolve away the PVA backing layer.

During imaging, a 488 nm laser was used to excite both Alexa 488 as well as FM 1-43. Alexa 647 was excited by a 639 nm laser. Three tracks were created for the PE substrate (Alexa 488, blue), polyimide (Alexa 647, red), and pig skin (FM 1-43FX, blue and green) respectively.

In-plane as well as thickness direction resolution was ~1 μm. Three dimensional confocal scanning results from bare pig skin and island-plus-serpentine EES on pig skin appear in Figs. S2B and S2C, respectively.

S3. Macroscopic mechanics models for interfacial delamination under tension/compression

The driving force for interfacial delamination between a PDMS film and a PE sheet subject to tensile strain ε in the PE can be obtained analytically as

$$G = \frac{\bar{E}_{\mathrm{PDMS}} h_{\mathrm{PDMS}} \bar{E}_{\mathrm{PE}} h_{\mathrm{PE}} \varepsilon^2}{2\left(1 - \frac{\bar{E}_{\mathrm{PDMS}} h_{\mathrm{PDMS}}}{\bar{E}_{\mathrm{PDMS}} h_{\mathrm{PDMS}} + \bar{E}_{\mathrm{PE}} h_{\mathrm{PE}}} \frac{L_{\mathrm{PDMS}}}{L_{\mathrm{PE}}}\right)^2} \frac{\bar{E}_{\mathrm{PDMS}} h_{\mathrm{PDMS}}^3 + \bar{E}_{\mathrm{PE}} h_{\mathrm{PE}}^3}{\left(\bar{E}_{\mathrm{PDMS}} h_{\mathrm{PDMS}}^2 - \bar{E}_{\mathrm{PE}} h_{\mathrm{PE}}^2\right)^2 + 4\bar{E}_{\mathrm{PDMS}} h_{\mathrm{PDMS}} \bar{E}_{\mathrm{PE}} h_{\mathrm{PE}} \left(h_{\mathrm{PDMS}} + h_{\mathrm{PE}}\right)^2} \tag{S2}$$

where $\bar{E}$, h and L are the plane-strain modulus, thickness and length of the corresponding layers. Equation (S2) is an extension of the steady-state driving force for interfacial delamination of a linear elastic bilayer to account for the finite lengths of PDMS film and PE sheet. FEM has been used to calculate the interfacial crack tip energy release rate. For relatively long delamination (much larger than h_{PDMS} and h_{PE}), FEM validates Eq. (S2) for a wide range of PDMS and PE elastic moduli and layer thickness. For short interfacial delamination ($\sim h_{\mathrm{PE}}$), the numerical results show similar dependence on the layer thickness as Eq. (S2), but are 2~2.5 times larger than Eq. (S2). The critical delamination strain is obtained once the driving force for interfacial delamination reaches the adhesion energy $\gamma_{\text{PDMS/PE}}$ between PDMS and PE. For 50:1 and 30:1 PDMS, the adhesion energy is 250 mJ/m^2 and 50 mJ/m^2, respectively.

For compression in the PE, initiation of interfacial delamination is more challenging to determine the case of tension because of compression on the interface. The large pre-stretch in the PE, as performed in experiments, prevents Euler-type buckling (to an arch shape). Therefore, increasing the compression induced in this manner eventually leads to wrinkling of the PDMS on PE. This behavior is similar to surface wrinkling of a semi-infinite solid subject to compression parallel to the surface *(33)*, but it is different in the following three aspects:

1) It involves two materials (PDMS and PE) such that the continuity of displacements and stress tractions must be enforced;
2) Both layers have finite thickness, and cannot be modeled as semi-infinite solids;
3) PE has large prestretch, which is not completely released during compression.

These features give the critical strain for wrinkling determined from the eigenvalue of a 8*8 matrix. The critical strain for wrinkling degenerates to *(33)* a semi-infinite solid.

S4. Microscopic mechanics models for contact between EES and skin

Microscopic mechanics models are developed to study contact between EES and skin, particularly on the effects of skin roughness, and device thickness and size. The skin morphology can be represented by a sinusoidal form $y(x)=h_{\text{rough}}\left[1+\cos\left(2\pi x/\lambda_{\text{rough}}\right)\right]/2$ with skin roughness amplitude h_{rough} and wavelength λ_{rough}. For non-conformal contact between EES and skin, EES does not follow the skin morphology and remains flat, which gives the total energy $\overline{U}_{\text{non-conformal}} = 0$. For conformal contact, both EES and skin deform such that the total displacement is $y(x)$. The displacements of EES and skin surface can be represented by $w(x) = h\left[1+\cos\left(2\pi x/\lambda_{\text{rough}}\right)\right]/2$ and $u_z(x) = \left(h_{\text{rough}} - h\right)\left[1+\cos\left(2\pi x/\lambda_{\text{rough}}\right)\right]/2$, respectively, where the maximum deflection *h* of EES is to be determined.

The total energy (*per unit length* along the wavelength direction) for conformal contact is $\overline{U}_{\text{conformal}} = \overline{U}_{\text{bending}} + \overline{U}_{\text{skin}} + \overline{U}_{\text{adhesion}}$, where the bending energy of EES is $\overline{U}_{\text{bending}} = \left(1/\lambda_{\text{rough}}\right)\int_0^{\lambda_{\text{rough}}} \left(\overline{EI}_{\text{EES}}/2\right)\left(w''\right)^2 dx = \pi^4 \overline{EI}_{\text{EES}} h^2/\lambda_{\text{rough}}^4$, the elastic energy of skin is $\overline{U}_{\text{skin}} \approx \pi \overline{E}_{\text{skin}} \left(h_{\text{rough}} - h\right)^2 / \left(16\lambda_{\text{rough}}\right)$, and the interfacial adhesion energy is $\overline{U}_{\text{adhesion}} = -\gamma \int_0^{\lambda_{\text{rough}}} \sqrt{1+\left(w'\right)^2}\, dx \approx -\gamma\left[1+\pi^2 h^2/\left(4\lambda_{\text{rough}}^2\right)\right]$. Minimization of the total energy then gives analytically the maximum deflection of EES $h = \overline{E}_{\text{skin}} h_{\text{rough}} / \left(16\pi^3 \overline{EI}_{\text{EES}}/\lambda_{\text{rough}}^3 + \overline{E}_{\text{skin}}\right)$.

Conformal contact requires $\overline{U}_{\text{conformal}} < \overline{U}_{\text{non-conformal}}$, which gives

$$\frac{4\pi^2 \overline{EI}_{\text{EES}}}{\gamma \lambda_{\text{rough}}^2} < \frac{4\lambda_{\text{rough}}^2}{h_{\text{rough}}^2 \pi^2}\left(\frac{16\pi^3 \overline{EI}_{\text{EES}}}{\overline{E}_{\text{skin}} \lambda_{\text{rough}}^3} + 1\right) + \frac{1}{\dfrac{16\pi^3 \overline{EI}_{\text{EES}}}{\overline{E}_{\text{skin}} \lambda_{\text{rough}}^3} + 1}. \tag{S3}$$

Since $\lambda_{\text{rough}} \sim 7h_{\text{rough}}$ in experiments (Fig. 2F), the second term on the right hand side is negligible and the above equation becomes

$$\frac{\pi \overline{E}_{\text{skin}} h_{\text{rough}}^2}{\gamma \lambda_{\text{rough}}} < 16 + \frac{\overline{E}_{\text{skin}} \lambda_{\text{rough}}^3}{\pi^3 \overline{EI}_{\text{EES}}}. \tag{S4}$$

For the FS-EES (Fig. 2B), $\overline{EI}_{\text{EES}} \approx 0.27 \times 10^{-9}$ N-m (SOM Section S5), $\overline{E}_{\text{skin}} \approx 130\ \text{kPa}$, $\lambda_{\text{rough}} \approx 140\ \mu\text{m}$, $\gamma \approx 0.16$ N/m (SOM Section S5), the above criterion implies that EES can have conformal contact with skin when the skin roughness is smaller than ~56 μm (Fig. 2G). This result is consistent with conformal contact observed in Fig. 2F (roughness in the range of 5~20 μm, as marked by the color bar in Fig. 2G).

For the island-plus-serpentine EES (Fig. S1D), the device is much thicker (Au 0.5 μm – PI 1.2 μm – Au 0.2 μm – PI 1.2 μm) and larger (500 μm×500 μm) than the FS strips (0.5 μm thick, 100 μm wide). For 400 μm spacing between adjacent islands (Fig. S1D), the effective bending stiffness is $\overline{EI}_{\text{EES}} \approx 1.6 \times 10^{-9}$ N-m from FEM, and the effective work of adhesion is $\gamma \approx 0.14$N/m (SOM Section S5). The criterion above implies that EES loses conformal contact once the skin roughness exceeds 27 μm, which is consistent with partial contact observed in the experiments for the range of skin roughness 20~50 μm (Fig. S2C).

For the FS-EES design, the effect of device thickness is studied by changing thicknesses of all layers proportionally. Let h_{device} denote the total thickness of device. Figure S10A shows that, for FS made of Au-PI as in experiments (red curve), the skin roughness for conformal contact decreases from ~56 μm to ~30 μm as the device thickness increases by 8 times. If all elastic moduli are proportionally reduced by 1000 times (blue curve), FS-EES would have conformal contact with much rougher skin. Therefore, thinner, softer devices promote conformal contact between EES and skin.

The thickness and modulus of the device and the skin roughness also play important roles on the comfort, or 'wearability', of EES. The contact pressure at the EES-skin interface is obtained analytically as *(34)*

$$\sigma_{\text{contact-global}} = \frac{8\pi^4 \bar{E}_{\text{skin}} h_{\text{rough}}}{16\pi^3 \lambda_{\text{rough}} + \frac{\bar{E}_{\text{skin}} \lambda_{\text{rough}}^4}{\overline{EI}_{\text{EES}}}} \cos\frac{2\pi x}{\lambda_{\text{rough}}}. \quad \text{(S5)}$$

Figure S10B (blue curve) shows the contact pressure between the FS-EES and skin of average roughness ($h_{\text{rough}} = 30\mu\text{m}$) for EES with device thickness of 0.5 μm. The maximum contact pressure is only 12.5 kPa, which is bellow the human skin sensitivity (~20kPa *(28)*) and therefore would not induce discomfort; devices thicker than 1.2 μm give a contact pressure higher than 20kPa, while devices thicker than 3.8 μm lose conformal contact to the skin. Larger skin roughness of 40 μm (red curve) results in higher interfacial pressure, and the device thickness to lose conformal contact becomes much smaller (~1.5μm). From Eq. (S5), it is obvious that softer device materials will give smaller contact pressure.

Figure S11 illustrates the mechanics model to determine the gap width *a* along the edges of EES. Since FS thickness h_{device} (~1 μm) is much smaller than that of the skin (~1 mm) and the PE (~30 μm) and the FS strip width (~100 μm), the FS between the skin and PE is analogous to inserting a rigid wedge of uniform thickness h_{device} at the skin/PE interface, leading to an interfacial crack *(35)*. The interfacial crack tip energy release rate is *(36)*

$$G \approx \frac{\left(\bar{E}_{\text{skin}} + \bar{E}_{\text{PE}}\right) h_{\text{device}}^2}{16\pi a}. \tag{S6}$$

The gap width a is obtained by G reaching the adhesion energy $\gamma_{\text{PE/skin}}$ as

$$a \approx \frac{\left(\bar{E}_{\text{skin}} + \bar{E}_{\text{PE}}\right) h_{\text{device}}^2}{16\pi\gamma_{\text{PE/skin}}}, \tag{S7}$$

which has been verified by FEM for the range of FS thickness in experiments.

The stress distribution $\sigma_{\text{contact-local}}$ over FS width is obtained analytically *(35)*, and is shown schematically in Fig. S11. The total force on FS strip is the integration of this $\sigma_{\text{contact-local}}$ and $\sigma_{\text{contact-global}}$ in Eq. (S4) over FS strip width, $F_{\text{total}} = \int_{FS\ width} \left(\sigma_{\text{contact-global}} + \sigma_{\text{contact-local}}\right) dx$, which has an average of -0.1 N/m for skin with $h_{\text{rough}} = 15$ μm and $\lambda_{\text{rough}} = 140$ μm.

S5. Effective work of adhesion between EES and skin, and effective bending stiffness of EES

The effective work of adhesion between EES and skin is given by

$$\gamma = \alpha\gamma_{\text{device-skin}} + \left(1-\alpha\right)\gamma_{\text{PE-skin}}, \tag{S8}$$

where α is the area fraction of devices, and $\gamma_{\text{device-skin}}$ and $\gamma_{\text{PE-skin}}$ are the work of adhesion for device-skin and PE-skin interfaces, respectively. Since adhesion between device (Au) and skin is very weak, Eq. (S8) is simplified to $\gamma \approx \left(1-\alpha\right)\gamma_{\text{PE-skin}}$. For the experimental value of $\gamma_{\text{PE-skin}} = 0.2\text{N/m}$ measured by rod-rolling set-up described in *(37)*, the effective work of adhesion is $\gamma \approx 0.16\text{N/m}$ for the FS-EES ($\alpha \approx 22.5\%$) and $\gamma \approx 0.14\text{N/m}$ for the island-plus-serpentine EES ($\alpha \approx 30.9\%$).

Similarly, for FS strips distributed over the entire surface of FS-EES electronics, the effective bending stiffness of EES is given by

$$\overline{EI}_{\text{EES}} = \alpha \overline{EI}_{\text{device}} + (1-\alpha)\overline{EI}_{\text{PE}}, \tag{S9}$$

where $\overline{EI}_{\text{PE}} = \overline{E}_{\text{PE}} h_{\text{PE}}^3 / 12$ is the bending stiffness of PE ($\overline{E}_{\text{PE}} = 65\text{kPa}$ and $h_{\text{PE}} = 30\mu\text{m}$ are the plane-strain modulus and thickness of PE, respectively), and the bending stiffness for PE with device is $\overline{EI}_{\text{device}} = \sum_{i=1}^{3} \overline{E}_i h_i \left[\left(b - \sum_{j=1}^{i} h_j \right)^2 + \left(b - \sum_{j=1}^{i} h_j \right) h_i + \frac{1}{3} h_i^2 \right]$ (where $b = \sum_{i=1}^{3} \overline{E}_i h_i \left(\sum_{j=1}^{i} h_j - \frac{1}{2} h_i \right) \Big/ \sum_{i=1}^{3} \overline{E}_i h_i$; $\overline{E}_1 = \overline{E}_{\text{PE}}$, $h_1 = h_{\text{PE}}$; $\overline{E}_2 = 2.8\text{GPa}$, $h_2 = 0.3\mu\text{m}$ are the plane-strain modulus and thickness for PI, respectively; and $\overline{E}_3 = 97\text{GPa}$, $h_3 = 0.2\mu\text{m}$ for Au). For $\alpha \approx 22.5\%$ from Fig. 2B, Eq. (S9) gives the effective bending stiffness 0.27×10^{-9} N-m, which agrees reasonably well with 0.30×10^{-9} N-m obtained by FEM.

S6. Sample fabrication of an FS-EES EP sensor

The sample fabrication begins with high temperature diffusion doping to define low resistance source and drain area for Ohmic contacts. Phosphorous spin-on-dopant (P509, Filmtronics, USA) was diffused at 950°C with constant supply of gas mixture (nitrogen:oxygen, 8:2). Transfer printing the resulting doped silicon nanomembrane to a handle wafer coated with PMMA/PI, followed by dry etching for isolation active regions, defined silicon areas on thin PI, as shown in Fig. 3A left frame. Electron-beam evaporation of metal (Cr/Au, 50/1500A) interconnects ground and output to the sensor and defines source, drain and gate electrodes (Fig. 3A right frame and its inset for a magnified view). Additional metallization for larger area sensor electrode, connection different layers through vias and second transfer printing to PE/PVA results in final sensor, as shown in Fig. S12.

S7. ECG measurement

The body ground electrode was a tin electrode filled with conductive gel, attached to the bony area on the right side of the subject’s right ankle. The EES was attached to the lower-left edge of the rib cage, near the left side of the midline of the chest. Usually one of the electrodes on the EES was used as reference electrode, while another was recording electrode. The negative end of the AA battery that powered the EES was also tied to the body ground. The gain of the main amplifier was 10000, with a high-pass frequency (HPF) of 0.1 Hz, and a low-pass-frequency (LPF) of 100 Hz. The sampling frequency was 1000Hz. A notch filter was applied in software to eliminate 60 Hz power line interference.

S8. EMG measurement from Leg

The EES was attached at about 1/3 the distance from the knee to the ankle, on the interior side of the left leg. Other parameters were the same as those for ECG, but with HPF= 0.01 Hz and LPF= 300 Hz. Passive measurements were done separately after recording with the EES, with otherwise exactly the same configurations. Two tin electrodes were attached in close vicinity of the EES, one on each side of it, vertically along the axis of extension of the muscle. The voltage differences between them were reported as the passive EMG.

S9. EMG measurement from Neck

The body ground electrode was attached to the right side of the subject's neck. The EES was attached at the skin overlying the cricothyroid muscle. The measurement parameters were the same as those for EMG on the leg.

S10. EEG measurement from forehead (alpha rhythms and Stroop effects)

Passive EES of both single channel design and multi-channel design have been tested in EEG measurements. For single channel design, the body ground and reference electrodes were commercial gold electrodes without using conductive gel, attached to the subject's left and right earlobes respectively. The EES was attached to the center of the subject's forehead without applying conductive gel, after exfoliating the skin slightly with scotch tapes. To test the multi-channel EES, one of the electrodes on it would be used as reference electrode, while another would be recording electrode. All other conditions were set up the same way as that of the single channel EES. The gain of the main amplifier was 10000, HPF= 0.01 Hz, LPF= 300 Hz. Sampling frequency was 1000 Hz. A notch filter was applied in software to eliminate 60 Hz power line interference.

S11. Simulated computer game control via neck EMG measured by EES

All computations were done in Matlab®. After eliminating 60 Hz interference from the raw data using an offline notch filter, the feature vector associated with each utterance was generated from the spectrogram of the data, using sliding window length of 256, overlap size of 250, and the fast-fourier transform (FFT) length of 512. Spectrograms were generated for an entire trial first, and then sliced into 750 ms intervals that correspond to the utterances of words, according to EMG onset times. These onset times were determined by an energy detecting procedure, where raw data were first sent through a high pass filter (Chebyshev type I, cutoff 70 Hz, high-pass 80 Hz), concatenated by a matched filter, and the signals were then squared. Whenever the power crossed a threshold value, a pair of onset and offset times of EMG activity was recorded.

In the original labeled dataset, there were 63 feature vectors for each of the 4 words. The metric of distance between any two feature vectors was the L1-norm, and dynamic time warping (DTW) was used to calculate the similarity score between them. In the computer game control demonstration, the user manipulated an avatar that can move in 4 directions in the game called Sokoban. In a simulated demonstration, when the user presses a key to signify the intended direction for the avatar, a candidate feature vector is randomly drawn from the EMG feature pool for that direction, and compared with all the rest of the feature vectors in all four pools as references, in terms of DTW scores. As a result, a nearest neighbor can be found for the candidate from one of the four pools, and it will be classified as a member from this nearest neighbor's group.

The classification accuracy depends on the number of reference feature vectors available for each direction (Fig S8). We have simulated (by resampling the data pool without replacement in 100 trials) the situation where various numbers of references were randomly available from each of the four pools, and found that the classification accuracy estimated across 100 trials increased with the number of references. When 62 references in each pool were used, the averaged accuracy could be higher than 95% for "up" and "down", and higher than 85% for "left" and "right". Thereby, the intended directions can be accurately classified and conveyed to the avatar, and gaming can thus be accomplished.

S12. DFT (discrete Fourier transform) coefficient

Given a vector of length N, $x[1],\cdots,x[N]$, the definition of the DFT coefficients, $X(k)$, is as follows.

$$X(k)=\sum_{j=1}^{N}x[j]\cdot\exp\left\{-\frac{2\pi i}{N}(j-1)(k-1)\right\}$$

Where $k=1,\cdots,N$

S13. Fatigue test

Repetitive stretching up to 1000 times with 30% tensile strain at 20 rpm shows no performance (resistance) degradation of FS electrodes, as shown in Fig. S13.

SOM Figure and Movie Captions

Fig. S1. (**A**) Stress-strain curve for a 30 μm thick free-standing PE film. The Young's modulus is 60 kPa. (**B**) Stress-strain curve for PVA. The Young's modulus is 1.9 GPa. (**C**) Stress-strain curve for 30:1 and 50:1 PDMS, with Young's moduli of 145 kPa and 19 kPa respectively. (D) Schematic illustration for a device island with size L_d and a serpentine span L_s. (**E**) Top view and cross-sectional schematic illustrations of an island-plus-serpentine sample. (**F**) Contour plot of strain in an island-plus-serpentine sample after stretching by 30%, computed using FEM.

Fig. S2. (**A**) Excitation and emission spectrum of fluorescent dyes used for confocal microscopy. Alexa Fluor 488 is used to stain PE substrate and Alexa Fluor 647 is used to stain polyimide, which is patterned into the layout of electrodes. Pig skin is stained by FM 1-43, which labels cell membrane. (**B**) Top and cross-sectional view of bare pig skin. (**C**) Top and cross-sectional view of EES with island mounted on pig skin.

Fig. S3. (**A**) Transfer curve and (**B**) IV curve of an Si MOSFET in FS geometry. (**C**) Calibration curve of a temperature sensor. (**D**) Percentage change in resistance of the strain gauge as a function of uniaxial tensile strain. Gauge factors for the longitudinal and transverse strain gauges are 1.3 and 0.5 respectively. (**E**) Proximity sensor and optical measurement system on skin using a combined LED-photodetector array with forward and reverse biases before (top frame) and after (bottom frame) deforming the skin with (left frame) and without (right frame) external illumination. (**F**) Current-voltage characteristics of a single LED. (**G**) Measured photocurrent from reverse biased diodes at different distances between the sensor and the external object. (**H**) Current and power of a FS Si photovoltaic cell at different voltages. (B) Images of an LC (inductor-capacitor) oscillator at 0% (left frame) and ~12% (right frame) tensile strain. (**J**) S21 of an LC oscillator as a function of frequency. The resonant frequency changes from 1.08 GHz (0% strain) to 1.38 GHz (~12% strain) due to tensile deformation.

Fig. S4. Magnified view of the EMG singal of Fig. 4B. Red and blue plots correspond to raw and high pass filtered data, respectively.

Fig. S5. (**A**) Images of an active EES-based EMG sensor on the neck without (left frame) and with (right frame) skin deformation. (**B**) Raw recordings from neck using a similar sensor for different words. “Go” (top frame), “Stop” (middle frame) and “Great” (bottom frame).

Fig. S6. EES EMG measurement from the neck for four different words, "up", "down", "left" and "right". Red and blue plots correspond to raw and high pass filtered data, respectively.

Fig. S7. Spectrograms of EES EMG measurements from the neck for four different words, “Go” (top frame), “Stop” (middle frame) and “Great” (bottom frame).

Fig. S8. Averaged classification accuracy versus the number of reference feature vectors available for classifying each direction. Shaded areas indicate one standard deviation of the data.

Fig. S9. (**A**) Recorded EEG data using passive EES sensor while eyes closed (top frame) and eyes open (bottom frame). (**B**) Experiment setup for Stroop test. When the target letter matches with its color (congruent case) the response speed is faster than the unmatched (incongruent) case.

Fig. S10. (**A**) Conformal contact requirement for FS-EES with devices of different thickness and modulus. (**B**) The contact pressure between the FS-EES and skin of different roughnesses.

Fig. S11. A schematic cross-sectional view of EES at the interface between skin and PE (top) and local stress distribution along the FS-EES/skin interface (bottom).

Fig. S12. Image of an FS-EES EP sensor on PE/PVA substrate.

Fig. S13. Fatigue test result for an FS-EES device under repetitive 20% tensile stretching.

Movie S1. A movie clip illustrating EES mounting procedure, deformations and extreme flexibility after detachment.

Movie S2. A movie clip showing an EES mounted on a commercial temporary transfer tattoo.

Movie S3. A movie clip illustrating delamination mechanics for soft, elastomeric films laminted onto human skin. PDMS (thickness 0.6 mm; modulus 14 kPa) or PE (thickness 0.3 mm; modulus of 60 kPa) films laminated on the wrist detach when the skin is stretched or wrinkled. By contrast, for EES devices (simulated here with a sheet of PE with 30 μm thickness) conformal contact is maintained under extreme deformations, due simply to the action of van der Waals forces.

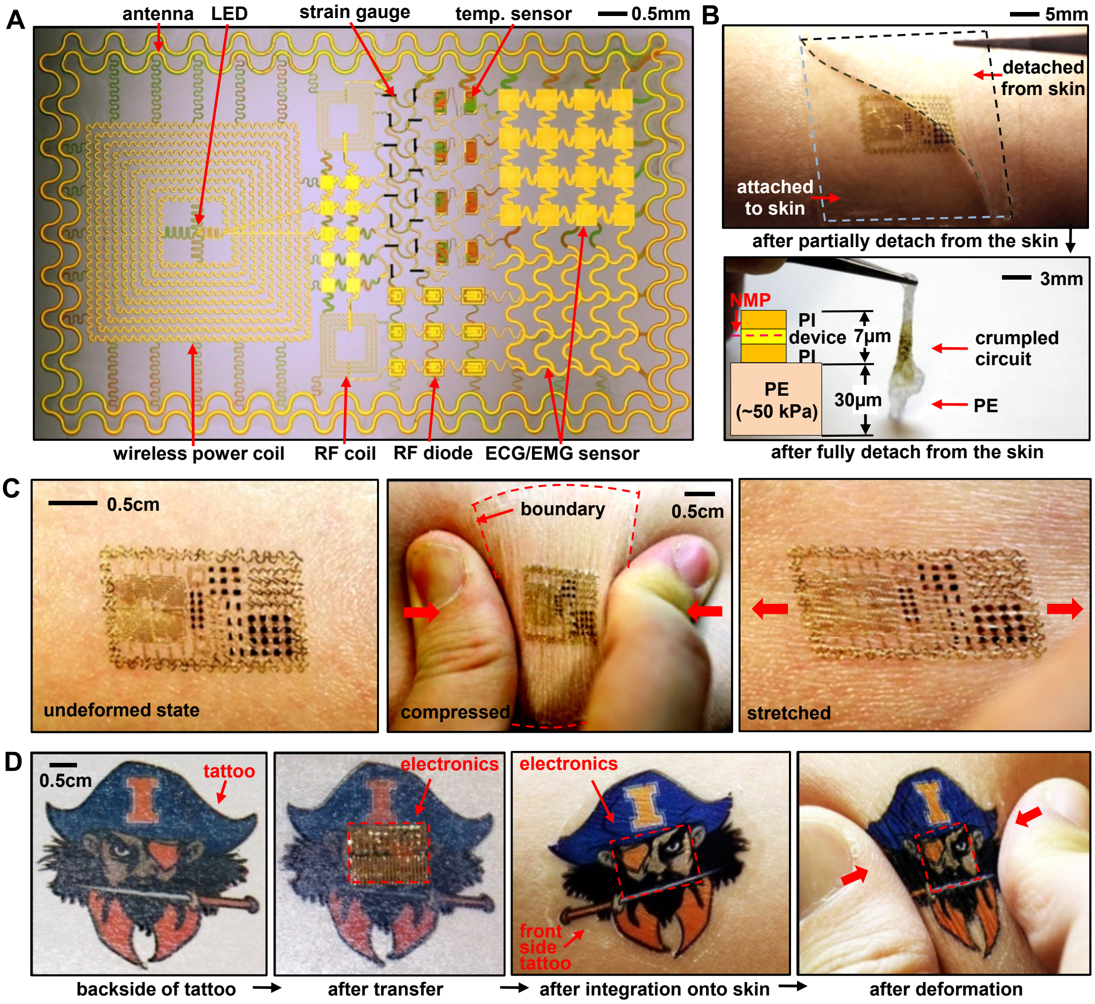
A
antenna
LED
strain gauge
temp. sensor
0.5mm
wireless power coil
RF coil
RF diode
ECG/EMG sensor
B
5mm
detached from skin
attached to skin
after partially detach from the skin
3mm
NMP
PI
device
PI
7μm
PE (~50 kPa)
30μm
crumpled circuit
PE
after fully detach from the skin
C
0.5cm
undeformed state
boundary
0.5cm
compressed
stretched
D
0.5cm
tattoo
backside of tattoo
electronics
after transfer
electronics
front side tattoo
after integration onto skin
after deformation

Figure 1

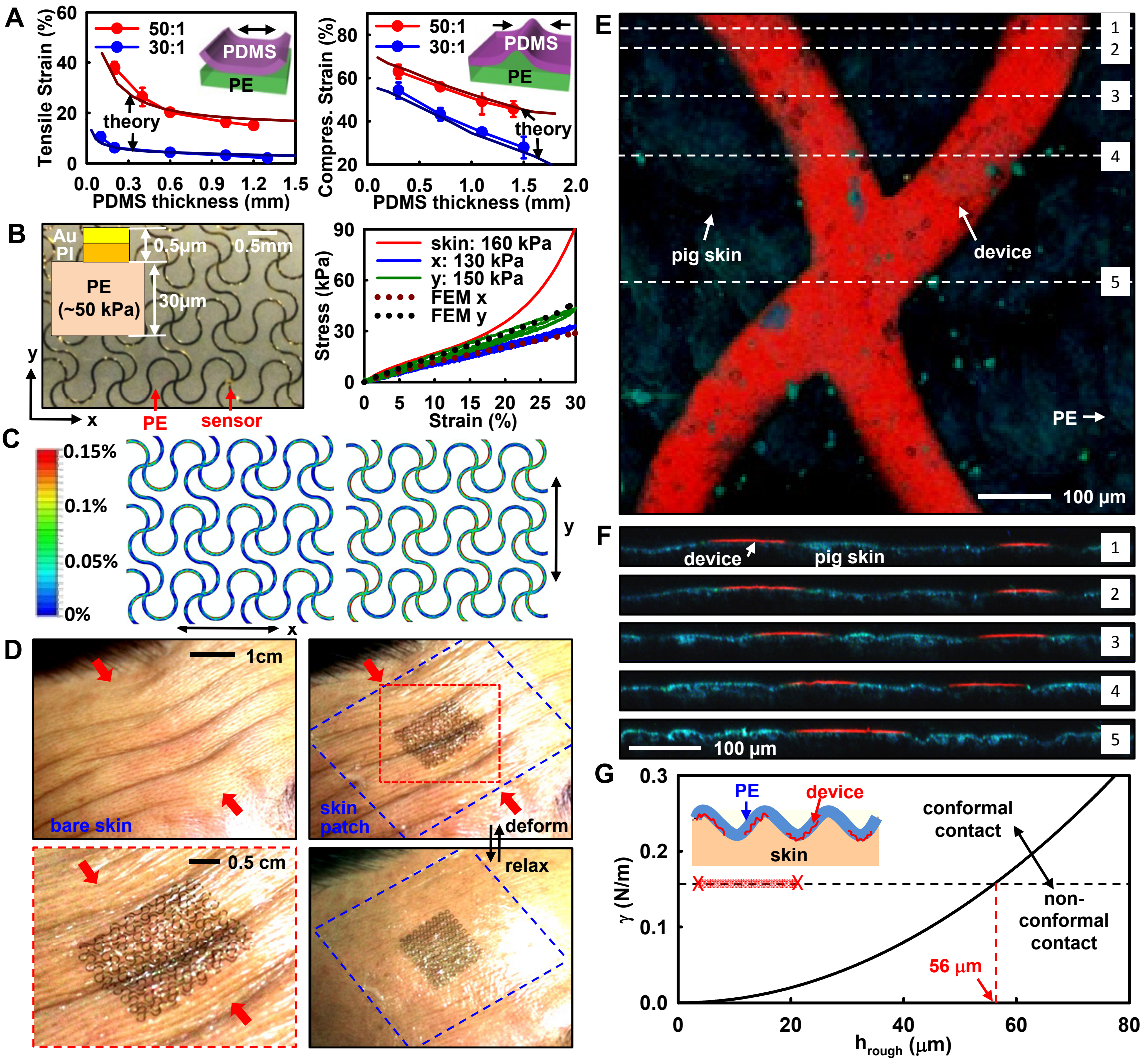
A
Tensile Strain (%)
60
40
20
0
50:1
30:1
PDMS
PE
theory
0.0 0.3 0.6 0.9 1.2 1.5
PDMS thickness (mm)
Compres. Strain (%)
80
60
40
20
50:1
30:1
PDMS
PE
theory
0.0 0.5 1.0 1.5 2.0
PDMS thickness (mm)
B
Au
PI
0.5μm
0.5mm
PE
(~50 kPa)
30μm
y
x
PE
sensor
Stress (kPa)
90
60
30
0
skin: 160 kPa
x: 130 kPa
y: 150 kPa
FEM x
FEM y
0 5 10 15 20 25 30
Strain (%)
C
0.15%
0.1%
0.05%
0%
y
x
D
1cm
bare skin
skin patch
deform
relax
0.5 cm
E
1
2
3
4
5
pig skin
device
PE
100 μm
F
device
pig skin
1
2
3
4
5
100 μm
G
0.3
0.2
0.1
0.0
γ (N/m)
PE
device
skin
conformal contact
non-conformal contact
56 μm
0 20 40 60 80
h_{rough} (μm)

Figure 2

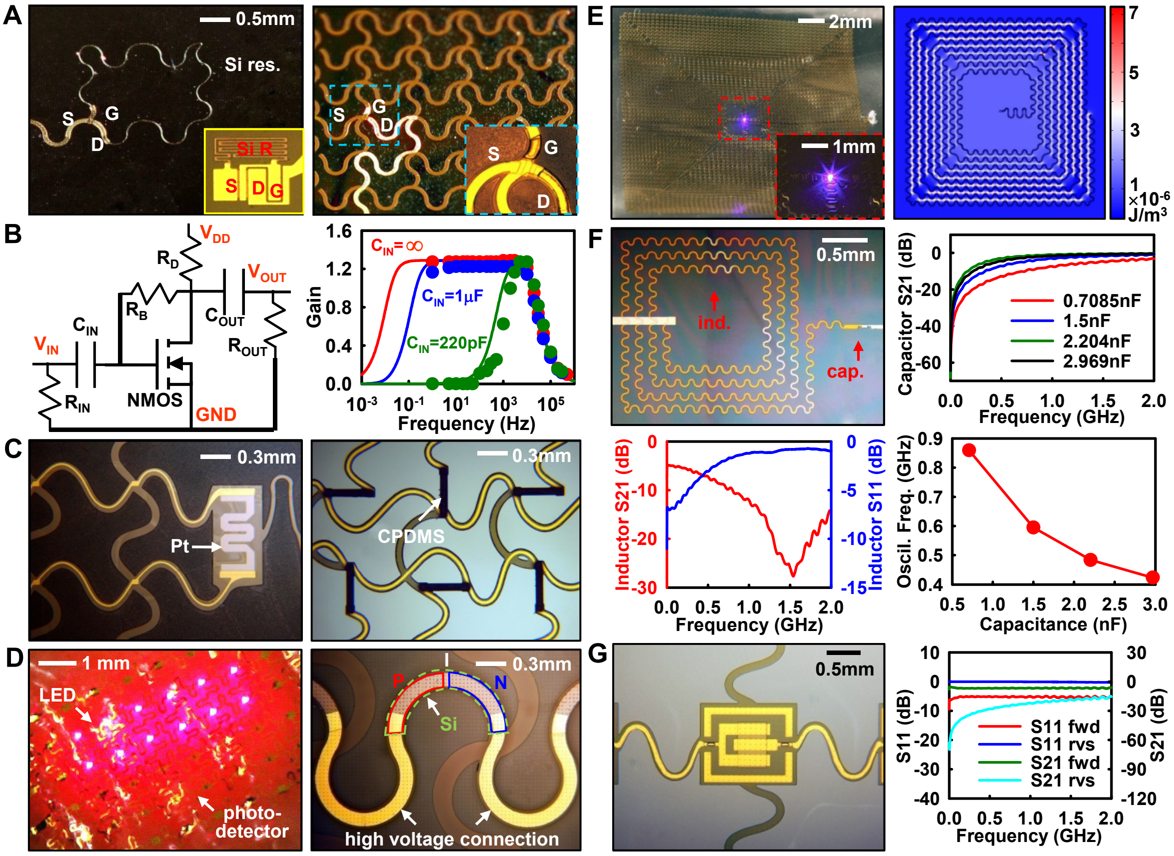
A
0.5mm
Si res.
S
G
D
Si R
S
D
G
S
G
D
S
G
D
B
V_{DD}
R_D
V_{OUT}
R_B
C_{IN}
C_{OUT}
V_{IN}
R_{OUT}
R_{IN}
NMOS
GND
1.6
1.2
0.8
0.4
0.0
Gain
$C_{IN}=\infty$
$C_{IN}=1\mu F$
$C_{IN}=220pF$
10^{-3}
10^{-1}
10^{1}
10^{3}
10^{5}
Frequency (Hz)
C
0.3mm
Pt
0.3mm
CPDMS
D
1 mm
LED
photo-detector
0.3mm
P
I
N
Si
high voltage connection
E
2mm
1mm
7
5
3
1
$\times10^{-6}$ J/m^3
F
0.5mm
ind.
cap.
Capacitor S21 (dB)
0
-20
-40
-60
0.7085nF
1.5nF
2.204nF
2.969nF
0.0
0.5
1.0
1.5
2.0
Frequency (GHz)
Inductor S21 (dB)
0
-10
-20
-30
Inductor S11 (dB)
0
-5
-10
-15
0.0
0.5
1.0
1.5
2.0
Frequency (GHz)
Oscil. Freq. (GHz)
0.9
0.8
0.7
0.6
0.5
0.4
0.5
1.0
1.5
2.0
2.5
3.0
Capacitance (nF)
G
0.5mm
S11 (dB)
10
0
-10
-20
-30
-40
S21 (dB)
30
0
-30
-60
-90
-120
S11 fwd
S11 rvs
S21 fwd
S21 rvs
0.0
0.5
1.0
1.5
2.0
Frequency (GHz)

Figure 3

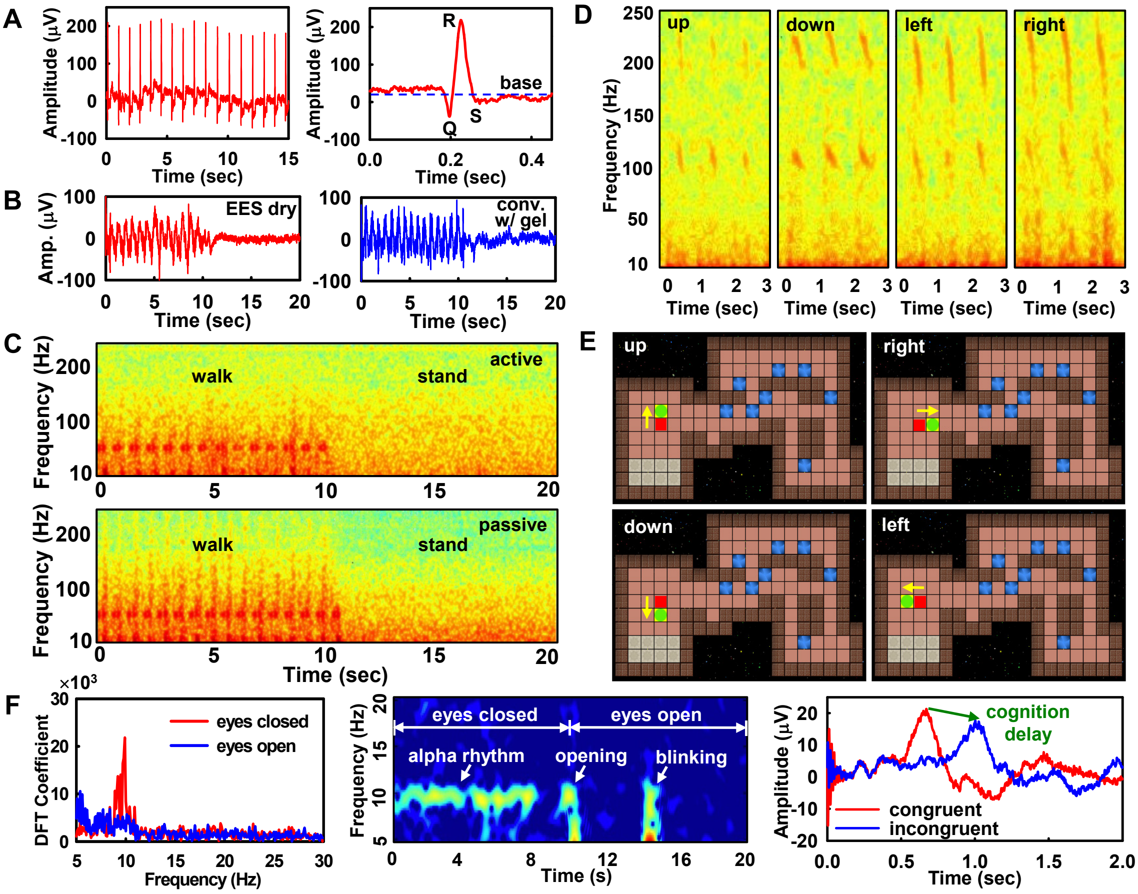
A
Amplitude (μV)
200
100
0
-100
0
5
10
15
Time (sec)
R
Q
S
base
0.0
0.2
0.4
B
Amp. (μV)
EES dry
conv. w/ gel
Time (sec)
C
Frequency (Hz)
walk
stand
active
passive
Time (sec)
D
up
down
left
right
Frequency (Hz)
250
200
150
100
50
10
Time (sec)
E
up
right
down
left
F
×10³
DFT Coefficient
eyes closed
eyes open
Frequency (Hz)
Frequency (Hz)
eyes closed
eyes open
alpha rhythm
opening
blinking
Time (s)
Amplitude (μV)
cognition delay
congruent
incongruent
Time (sec)

Figure 4

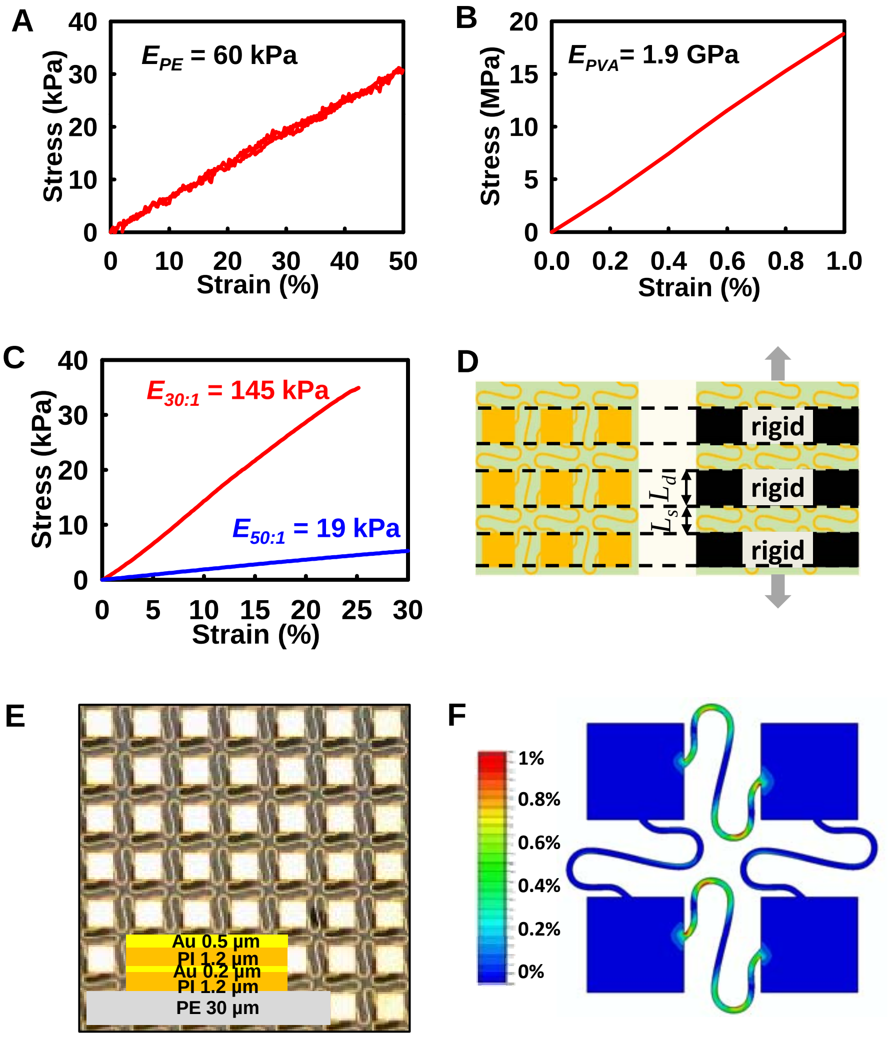
A
Stress (kPa)
40
30
20
10
0
0
10
20
30
40
50
Strain (%)
E_{PE} = 60 kPa
B
Stress (MPa)
20
15
10
5
0
0.0
0.2
0.4
0.6
0.8
1.0
Strain (%)
E_{PVA}= 1.9 GPa
C
Stress (kPa)
40
30
20
10
0
0
5
10
15
20
25
30
Strain (%)
$E_{30:1}$ = 145 kPa
$E_{50:1}$ = 19 kPa
D
rigid
rigid
rigid
L_d
L_s
E
Au 0.5 μm
PI 1.2 μm
Au 0.2 μm
PI 1.2 μm
PE 30 μm
F
1%
0.8%
0.6%
0.4%
0.2%
0%

Figures S1

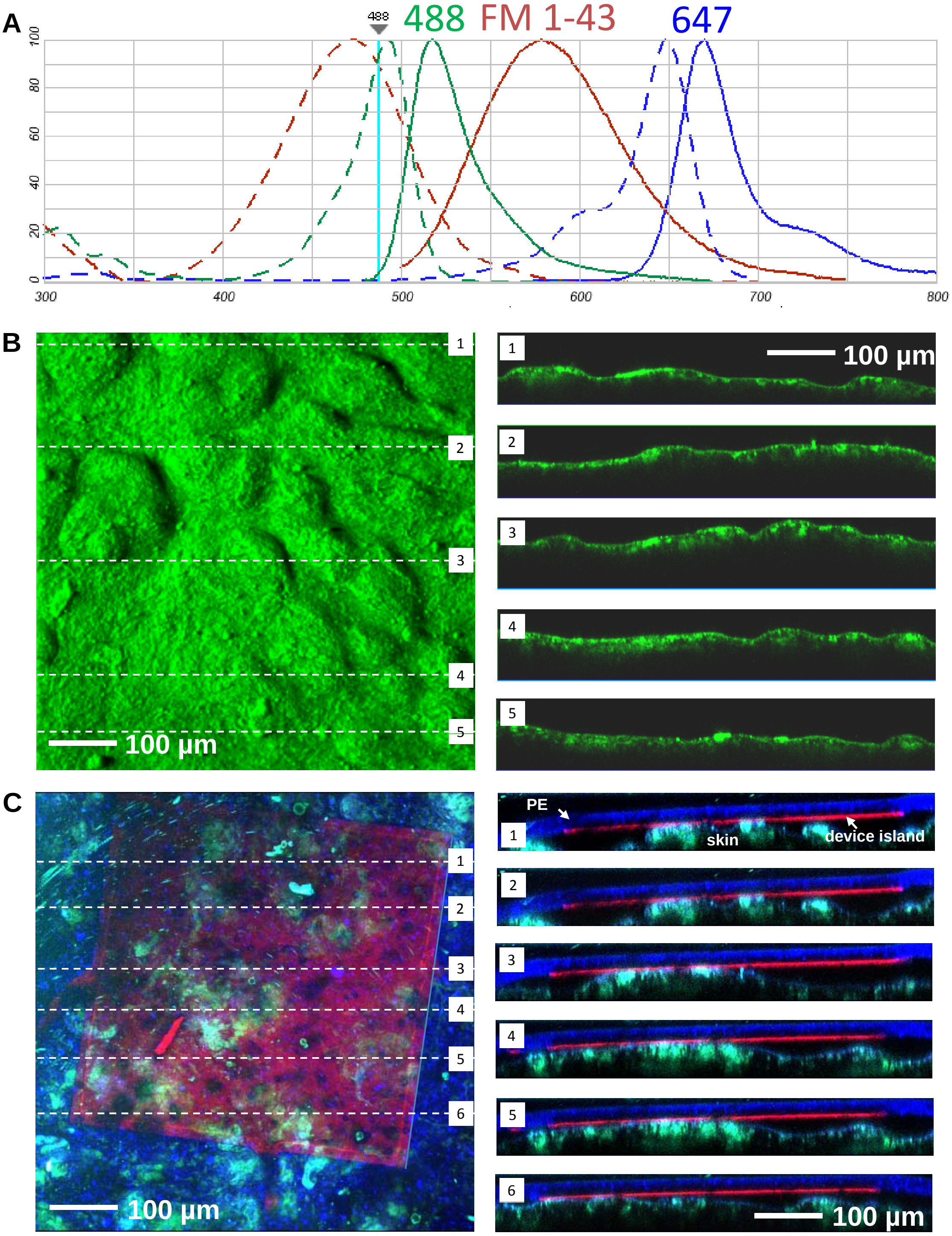
A
488
488
FM 1-43
647
0
20
40
60
80
100
300
400
500
600
700
800
B
1
2
3
4
5
100 µm
100 µm
C
1
2
3
4
5
6
100 µm
PE
skin
device island
100 µm

Figures S2

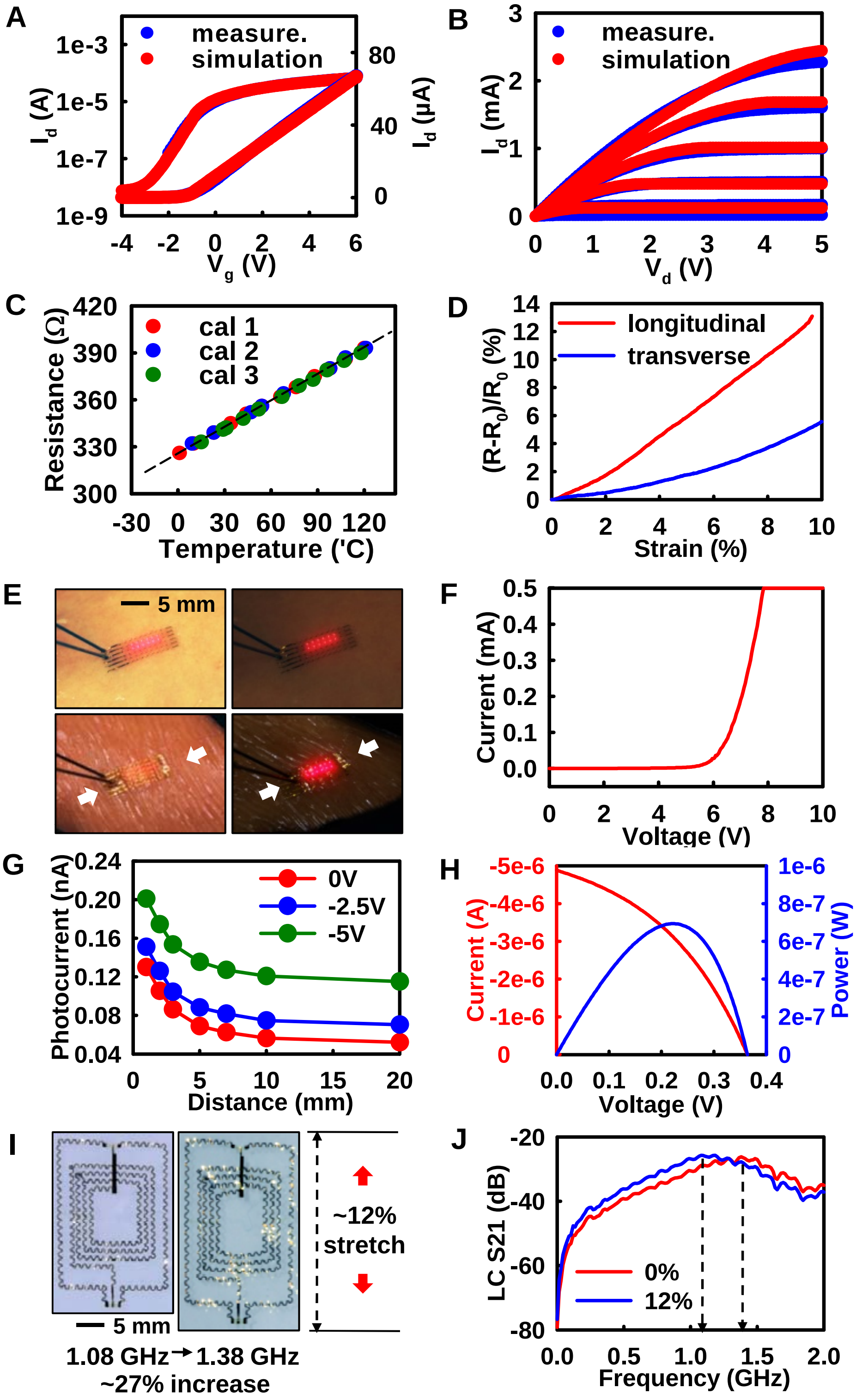
A
measure.
simulation
1e-3
1e-5
1e-7
1e-9
I_d (A)
80
40
0
I_d (μA)
-4 -2 0 2 4 6
V_g (V)
B
measure.
simulation
3
2
1
0
I_d (mA)
0 1 2 3 4 5
V_d (V)
C
cal 1
cal 2
cal 3
420
390
360
330
300
Resistance (Ω)
-30 0 30 60 90 120
Temperature ('C)
D
longitudinal
transverse
14
12
10
8
6
4
2
0
$(R-R_0)/R_0$ (%)
0 2 4 6 8 10
Strain (%)
E
5 mm
F
0.5
0.4
0.3
0.2
0.1
0.0
Current (mA)
0 2 4 6 8 10
Voltage (V)
G
0V
-2.5V
-5V
0.24
0.20
0.16
0.12
0.08
0.04
Photocurrent (nA)
0 5 10 15 20
Distance (mm)
H
-5e-6
-4e-6
-3e-6
-2e-6
-1e-6
0
Current (A)
1e-6
8e-7
6e-7
4e-7
2e-7
0
Power (W)
0.0 0.1 0.2 0.3 0.4
Voltage (V)
I
~12%
stretch
5 mm
1.08 GHz→1.38 GHz
~27% increase
J
-20
-40
-60
-80
LC S21 (dB)
0%
12%
0.0 0.5 1.0 1.5 2.0
Frequency (GHz)

Figures S3

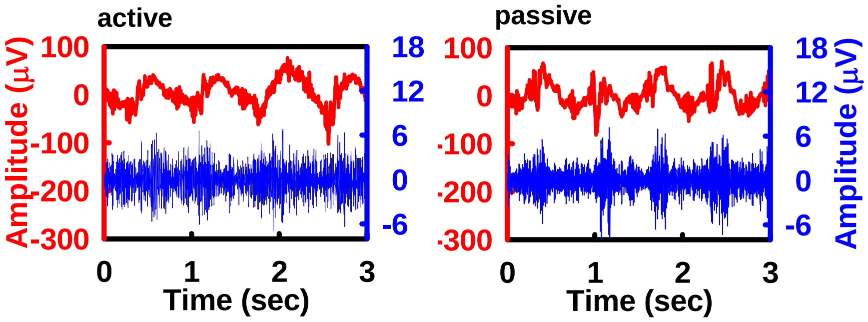
active
passive
Amplitude (μV)
100
0
-100
-200
-300
18
12
6
0
-6
Amplitude (μV)
0
1
2
3
Time (sec)
Time (sec)

Figures S4

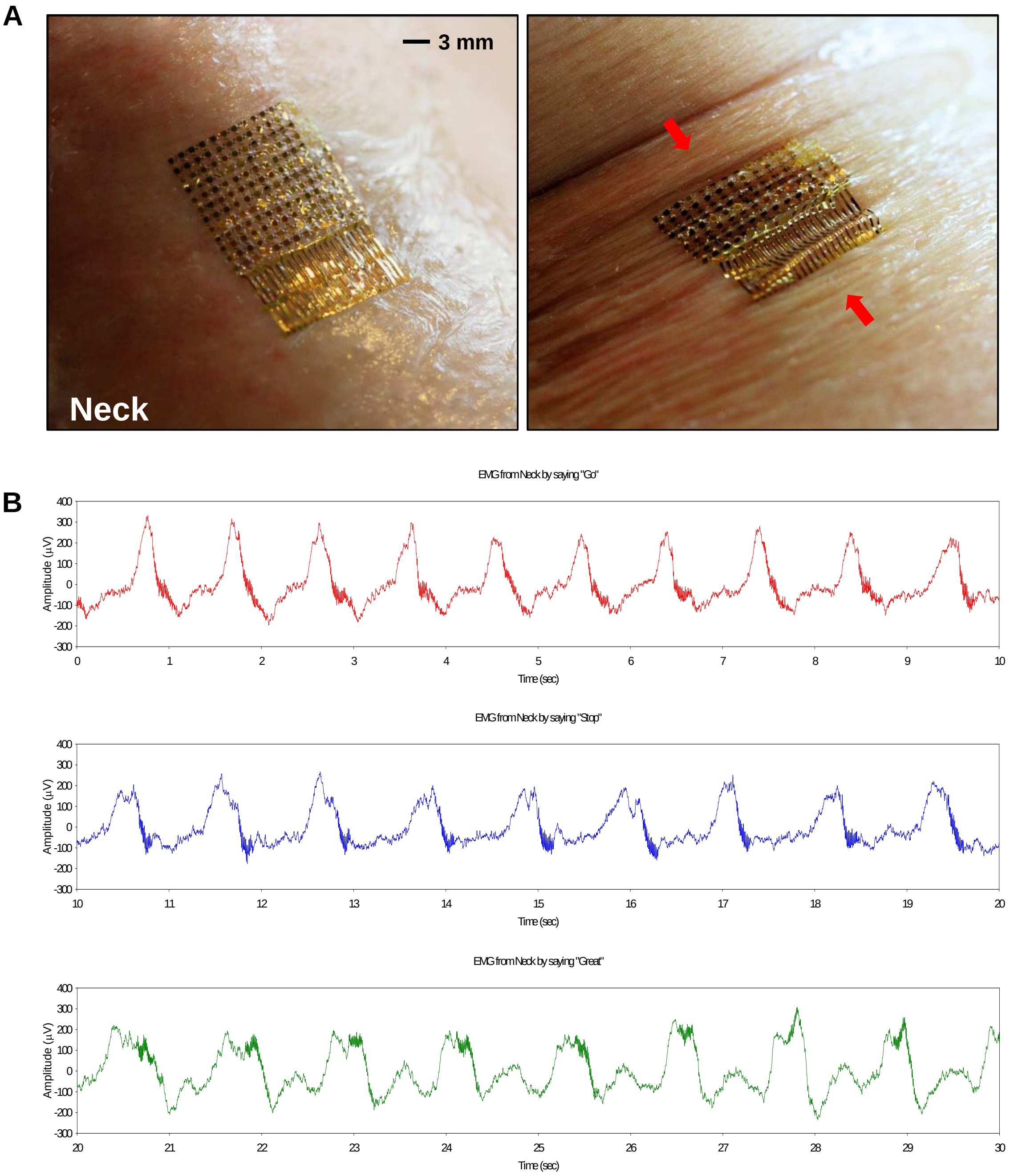
A
3 mm
Neck
B
EMG from Neck by saying "Go"
Amplitude (μV)
400
300
200
100
0
-100
-200
-300
0
1
2
3
4
5
6
7
8
9
10
Time (sec)
EMG from Neck by saying "Stop"
Amplitude (μV)
400
300
200
100
0
-100
-200
-300
10
11
12
13
14
15
16
17
18
19
20
Time (sec)
EMG from Neck by saying "Great"
Amplitude (μV)
400
300
200
100
0
-100
-200
-300
20
21
22
23
24
25
26
27
28
29
30
Time (sec)

Figures S5

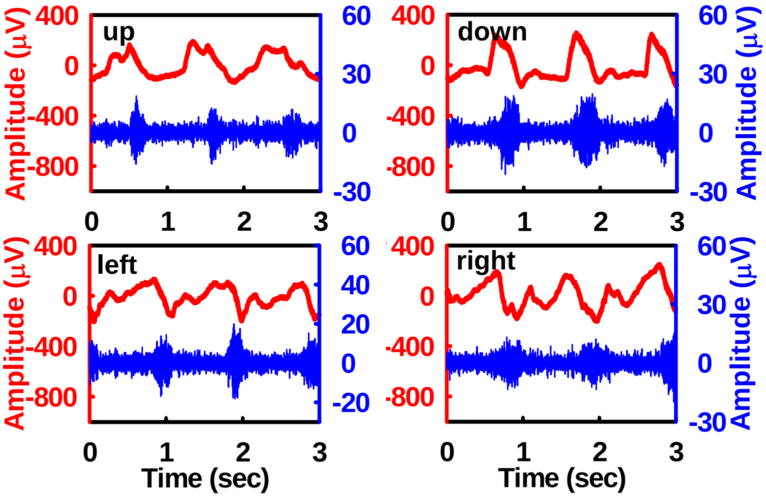

up
down
left
right
400
0
-400
-800
60
30
0
-30
40
20
-20
Amplitude (μV)
0
1
2
3
Time (sec)

Figures S6

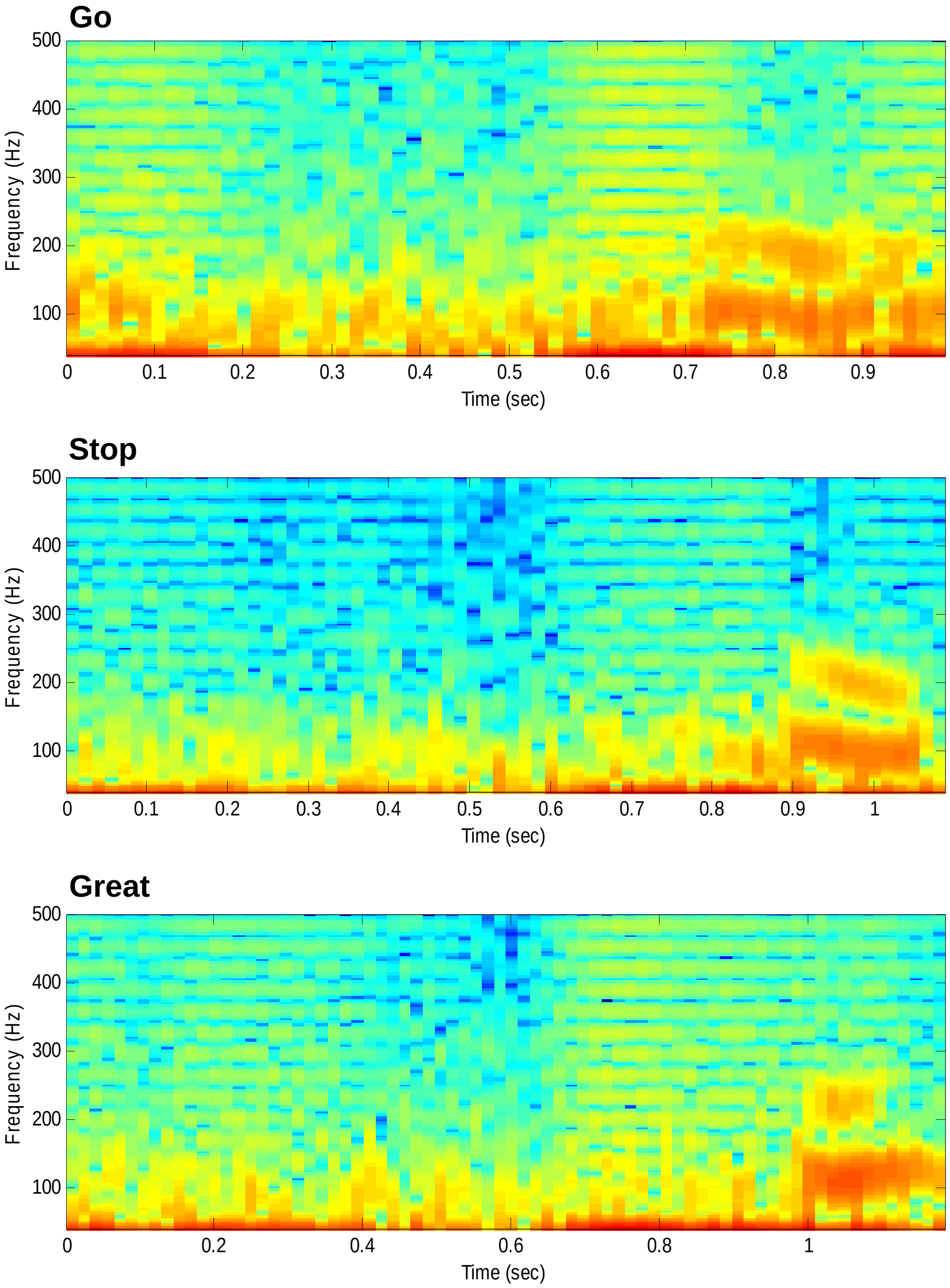

Go

Stop

Great

Figures S7

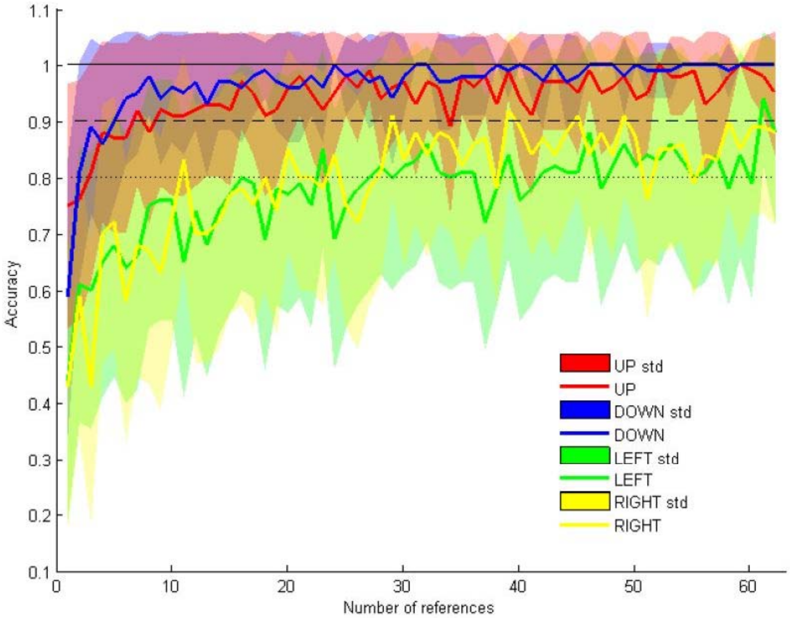
1.1
1
0.9
0.8
0.7
0.6
0.5
0.4
0.3
0.2
0.1
Accuracy
0
10
20
30
40
50
60
Number of references
UP std
UP
DOWN std
DOWN
LEFT std
LEFT
RIGHT std
RIGHT

Figures S8

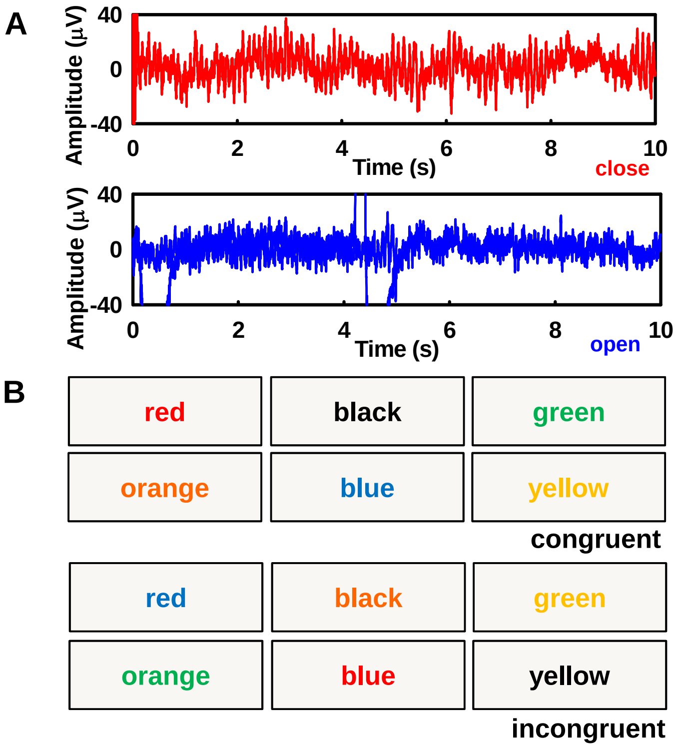
A
Amplitude (µV)
40
0
-40
0
2
4
6
8
10
Time (s)
close
Amplitude (µV)
40
0
-40
0
2
4
6
8
10
Time (s)
open
B
red
black
green
orange
blue
yellow
congruent
red
black
green
orange
blue
yellow
incongruent

Figures S9

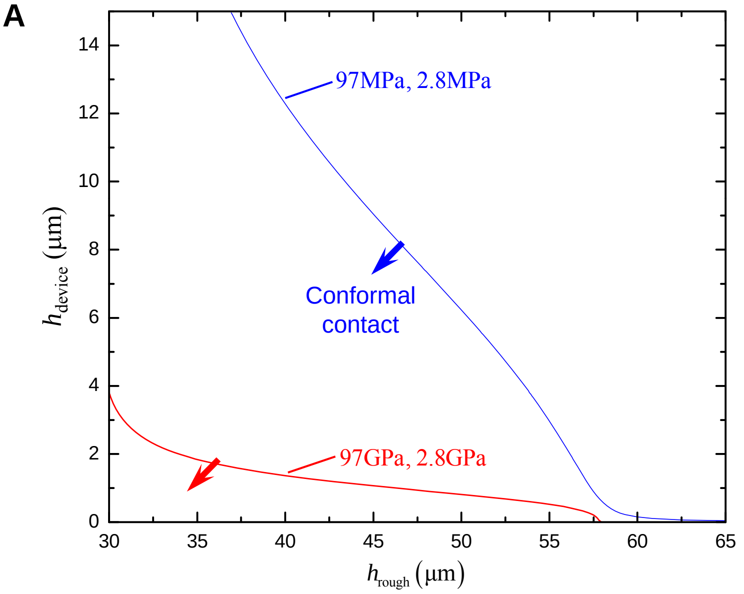
A
h_{device} (μm)
14
12
10
8
6
4
2
0
30
35
40
45
50
55
60
65
h_{rough} (μm)
97MPa, 2.8MPa
Conformal contact
97GPa, 2.8GPa

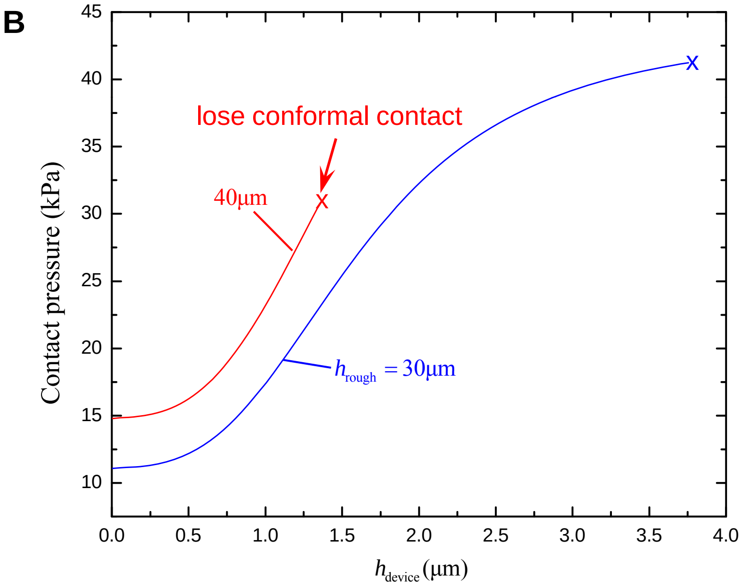
B
Contact pressure (kPa)
45
40
35
30
25
20
15
10
0.0
0.5
1.0
1.5
2.0
2.5
3.0
3.5
4.0
h_{device} (μm)
lose conformal contact
40μm
x
x
h_{rough} = 30μm

Figures S10

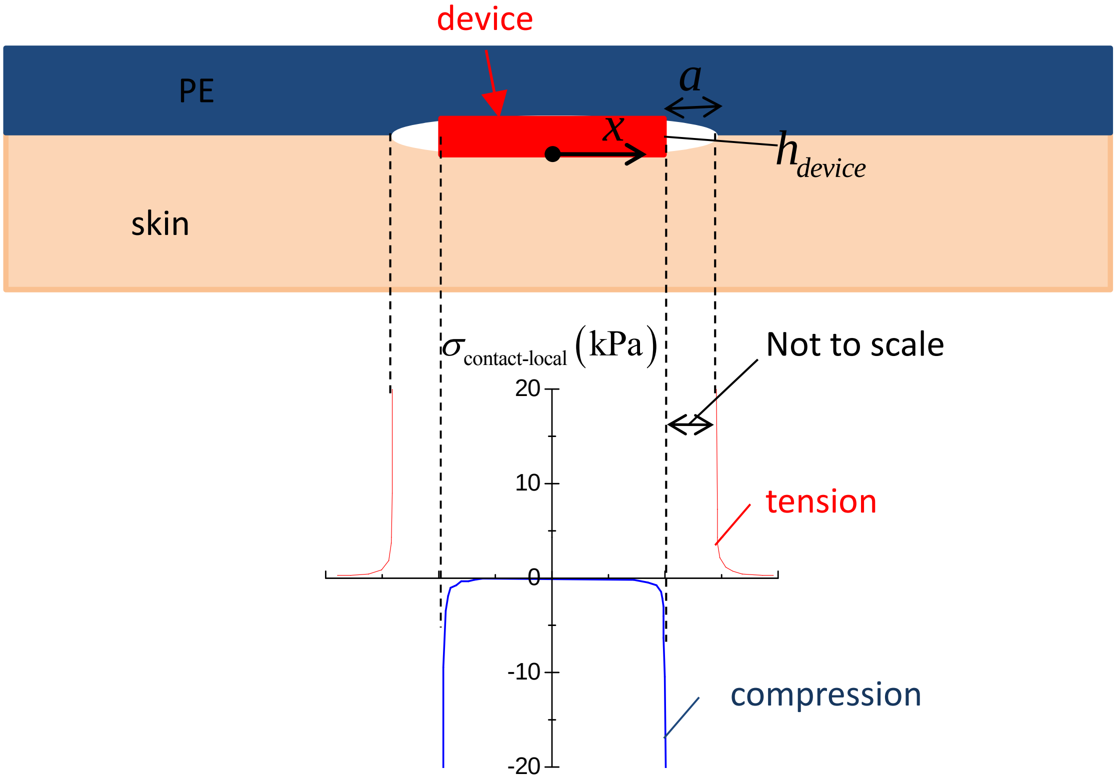
device
PE
a
x
h_{device}
skin
$\sigma_{\text{contact-local}}\,(\text{kPa})$
Not to scale
20
10
0
-10
-20
tension
compression

Figures S11

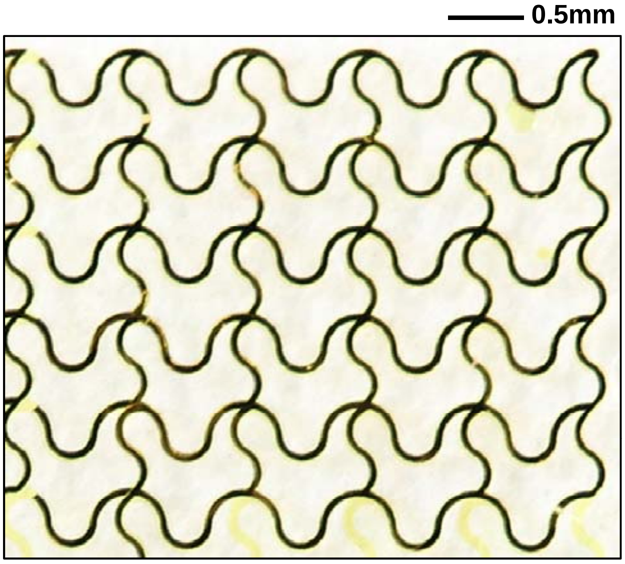

Figures S12

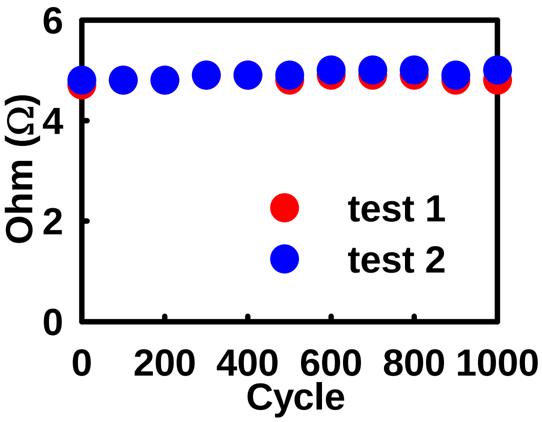

Figures S13